Marine Micropaleontology 191 (2024) 102390

Contents lists available at ScienceDirect

Marine Micropaleontology

journal homepage: www.elsevier.com/locate/marmicro

Integrated record of the Late Lutetian Thermal Maximum at IODP site U1508, Tasman Sea: The deep-sea response

Irene Peñalver-Clavel [a,*], Claudia Agnini [b], Thomas Westerhold [c], Marlow J. Cramwinckel [d], Edoardo Dallanave [e,1], Joyeeta Bhattacharya [f], Rupert Sutherland [g], Laia Alegret [a]

[a] Departamento de Ciencias de la Tierra & IUCA, Universidad de Zaragoza, Zaragoza, Spain
[b] Dipartimento di Geoscienze, Università degli Studi di Padova, Padova, Italy
[c] MARUM - Center for Marine Environmental Sciences, University of Bremen, Germany
[d] Department of Earth Sciences, Faculty of Geosciences, Utrecht University, the Netherlands
[e] Deparment of Geosciences, University of Bremen, Germany
[f] Picarro Inc. Headquarters, Santa Clara, California, USA
[g] School of Geography, Environment and Earth Sciences, Victoria University of Wellington, New Zealand

ARTICLE INFO

Keywords:
Eocene
SW Pacific
Hyperthermal
Benthic foraminifera
C19r event
Geochemistry

ABSTRACT

The Late Lutetian Thermal Maximum (LLTM) was a transient and brief global warming event recorded in the middle Eocene, at 41.52 Ma. The biotic response to the LLTM has been documented at only a few marine sites so far. Here, we present the first record of deep-sea benthic foraminiferal assemblage changes during the LLTM in the southwest Pacific at International Ocean Discovery Program Hole U1508C (1609 m water depth) in the Tasman Sea. The LLTM coincides with a negative excursion in bulk sediment δ^{13}C (0.47‰) and benthic foraminifera δ^{13}C (0.36‰), with changes in the relative abundance of benthic foraminiferal species and in the deep-water organic geochemistry. The decrease in diversity of the assemblages indicates environmental stress during the event, potentially linked to oxygen deficiency, as evidenced by the occurrence of dysoxic taxa (e.g. *Lenticulina* spp., *Turrillina brevispira)*. Although calcareous taxa dominate, the presence of corrosion-resistant species and poorly preserved foraminiferal tests suggest slightly $CaCO_3$-corrosive bottom waters, but no dissolution was evident. We suggest the shallowing of the thermocline and enhanced water column stratification at this site during the LLTM.

1. Introduction

The climate of the middle to late Eocene has been described as a warmhouse state with a gradual cooling trend towards the Eocene/Oligocene transition (Westerhold et al., 2020). This cooling trend was interrupted by short-lived warming events, documented by negative excursions in carbon and oxygen isotope records (e.g. Wade and Kroon, 2002; Bohaty and Zachos, 2003). Some of these have been described as hyperthermal events (e.g. Thomas et al., 2000; Foster et al., 2018). Hyperthermals are typically associated with increased global temperature, high pCO_2 levels (e.g. Bijl et al., 2010; Pearson, 2010) and marine carbonate dissolution (e.g. Leon-Rodriguez and Dickens, 2010; Sexton et al., 2011; Bhattacharya and Dickens, 2020), and they are considered to be indicative of perturbations of the global carbon cycle (e.g. Lyle et al., 2005; Rivero-Cuesta et al., 2020).

The Late Lutetian Thermal Maximum (LLTM), also known as “C19r event” (Edgar et al., 2007), was a middle Eocene hyperthermal event ocurring at ∼ 41.52 Ma, within the upper part of magnetic polarity Chron C19r (Westerhold and Röhl, 2013). In the South Atlantic Ocean, the carbon isotope excursion (CIE) associated with the LLTM spans only 30 kyr, making it relatively short compared to the frequent hyperthermals of the early Eocene; the clay layer of maximum carbonate dissolution represents only 5 kyr, and the period of 2 °C warming in the deep-sea lasted 10 kyr (Westerhold et al., 2018). This very short time-span makes it difficult to identify the LLTM in deep-sea sediments.

While other hyperthermal events have been associated with periods of elevated pCO_2 levels, the LLTM warming has been linked to the highest insolation values of the last 45 million years on Earth’s surface,

---

* Corresponding author at: Departamento de Ciencias de la Tierra & IUCA, Universidad de Zaragoza, Zaragoza, Spain.
E-mail address: irenepc@unizar.es (I. Peñalver-Clavel).

[1] Now at the Department of Earth Sciences, University of Milan (Italy)

https://doi.org/10.1016/j.marmicro.2024.102390
Received 31 May 2024; Received in revised form 31 July 2024; Accepted 1 August 2024
Available online 2 August 2024

along with an accelerated hydrological cycle (Westerhold and Röhl, 2013; Intxauspe-Zubiaurre et al., 2018; Westerhold et al., 2018). Studying the biotic response to intensified insolation, and the subsequent planetary warming, provides valuable insights into ecological dynamics during such extreme climate events. However, only a few studies are available, and these are focused on the Atlantic Ocean. In the South Atlantic, the LLTM has been documented at Ocean Drilling Program (ODP) Sites 702, 1260 and 1263 (Edgar et al., 2007; Westerhold and Röhl, 2013; Westerhold et al., 2018; Rivero-Cuesta et al., 2020). In the northeast Atlantic, it has been reported from the Spanish Cape Oyambre section in the Basque-Cantabric Basin (Intxauspe-Zubiaurre et al., 2018). These studies record the negative excursion in carbon and oxygen stable isotopes, with a CIE of 0.47 ‰ in bulk sediment and 0.36 ‰ in benthic foraminifera, and an OIE of 0.45 ‰ in bulk sediment and 0.48 ‰ in benthic foraminifera, respectively. Additionally, a decrease of ~15 % in $CaCO_3$ content is recorded. Benthic foraminifera provide one of the best deep-sea fossil records during the Cenozoic, and they are an excellent tool to reconstruct palaeoenvironmental conditions during the Paleogene (Alegret et al., 2021a; Arreguín-Rodríguez et al., 2022), including the transition from the middle Eocene warmhouse state to the early Oligocene coolhouse climate state (e.g. Thomas, 1992; Ortiz and Thomas, 2015). Their response to the largest hyperthermal event of the Paleogene, the Paleocene-Eocene Thermal Maximum (PETM), has been widely documented, and multiple studies have analysed their faunal turnover across early Eocene hyperthermal events, but few of them have considered the hyperthermals that punctuated the gradual cooling trend of the middle Eocene (Intxauspe-Zubiaurre et al., 2018; Arreguín-Rodríguez et al., 2022). So far, the benthic foraminiferal response to the LLTM has only been studied at ODP Site 702 (lower bathyal depths, 1000–2000 m; Rivero-Cuesta et al., 2020) and at Cape Oyambre section, situated on a continental margin setting (middle bathyal depths, 600–1000 m; Intxauspe-Zubiaurre et al., 2018). At both sites, negative CIE and OIE were recorded along with a decrease in carbonate content in deep-sea sediments during the event. Additionally, a decrease in diversity (but no extinctions) and temporary shifts in species abundance among benthic foraminifera were observed (Intxauspe-Zubiaurre et al., 2018; Rivero-Cuesta et al., 2020).

Here, we present the first record of deep-sea benthic foraminifera across the LLTM in the southwest Pacific. International Ocean Discovery Program (IODP) Expedition 371 in the Tasman Sea provided a unique Eocene sedimentary record in a key location for understanding the palaeoceanographic and palaeoclimatic evolution of the southwest Pacific (Sutherland et al., 2019). Quantitative analyses of benthic foraminiferal assemblages are used to document the response of deep-sea ecosystems to a rapid warming event associated with a global disturbance of the carbon cycle, with implications for studies that calibrate the response of the benthos to hyperthermal events of different magnitude and background climate states (e.g., Arreguín-Rodríguez et al., 2022). We compare our results with the four other locations in the Atlantic Ocean where the LLTM has been documented.

2. Location and geological setting

Site U1508 (34°26.89′S, 171°20.59′E; 1609 m water depth) was drilled during IODP Expedition 371 in the Tasman Sea, southwest Pacific Ocean, ~130 km west of Cape Reinga, which is the northern tip of the Northland region of northern New Zealand (Fig. 1A) (Sutherland et al., 2019). It is located in the Reinga Basin, a topographic depression within the continental crust of Zealandia (Mortimer et al., 2017; Sutherland et al., 2020). The Reinga Basin currently has water depths of 1500–2500 m, and is bounded by Reinga Ridge and South Maria Ridge to the northeast, by the West Norfolk Ridge to the west, and it is continuous with Northland basin to the southeast (Fig. 1B).

At present, Site U1508 lies at the southern extent of the southeast-flowing East Australian Current (often referred to as Tasman Front), which is the subtropical return flow of the South Pacific Gyre (Fig. 1A). Site U1508 penetrated a total of ~700 m of Pleistocene to lower Eocene heterogeneous sediments (Sutherland et al., 2019). Seafloor sediment at Site U1508 is composed of clayey nannofossil chalk and nannofossil limestone with foraminiferal and bryozoan fragments (Sutherland et al., 2019).

Local palaeogeographic information is synthesized in Fig. 2B. Site U1508 at 41 Ma is inferred to have been at lower bathyal depths on a saddle that connected New Caledonia Trough and Aotea Basin to a deeper basin that lay north of Reinga Basin at that time (and has since been subducted). The estimated palaeolatitude of the site was ~47°S (Fig. 2B) (Dallanave et al., 2022). During the Eocene, ocean-atmosphere models suggest a precursor to the South Pacific Gyre acted as a significant global driver of ocean heat transport (Huber et al., 2004). However, the intensity of the gyre was lower compared to today conditions, because the ocean gateway between Australia and Antarctica did not fully open until the end of the Eocene, and the gyre intensified as the Southern Ocean became wider and Antarctica colder (Kennett, 1977). Even so, the southwest Pacific Ocean was the main source of intermediate and deep-water formation during the early Paleogene (Sijp et al., 2014; Baatsen et al., 2020).

We suggest that, similar to today, the Zealandia continent represented a natural barrier for the flowing of ocean currents and was bounded on its northern side (near Site U1508, Fig. 2B) by a southeast-flowing precursor to the Eastern Australian Current (EAC, Fig. 2A), and on its southern side by the northward-flowing Tasman Current (TC) (Huber et al., 2004; Cramwinckel et al., 2020) (Fig. 2A). Flowing along the east of the Australian coast at surface and intermediate levels, the EAC was a warm, saline and nutrient-poor water mass that flowed southward, while the TC was a relatively cool wind-driven current that flowed northward along the east of the Australian coast (Huber et al., 2004; Bijl et al., 2011).

3. Material and methods

The study interval in Hole 1508C ranges from Core 22R, Section 1, interval 15–16 cm (560.96 m CSF-A) to Core 22R, Section 5, interval 127–128 cm (567.40 m CSF-A), and consists of moderately bioturbated nannofossil chalk and nannofossil limestone with foraminifera (Sutherland et al., 2019).

Our refined age model based on a magneto-biochronological framework integrated with available bulk sediment isotopic data from Hole U1508C (Bhattacharya, 2021) and the reference high-resolution isotopic record from the Atlantic Ocean (Westerhold et al., 2018), allowed us to identify the short-lived LLTM and to plan the sampling strategy for benthic foraminiferal studies.

3.1. Inorganic geochemistry

Carbon and oxygen stable isotopes were measured on bulk sediment and benthic foraminifera (Fig. 3) in a total of 32 samples, taken between 560.96 and 567.40 m CSF-A, at MARUM Isotope Laboratory (Bremen University). Sampling resolution ranged from 0.05 to 0.41 m CSF, resulting in time resolution varying from 2 to 20 kyr (Suppl. Table S1).

Specimens of *Nuttallides truempyi* were used for species-specific isotope analyses on benthic foraminifera, and bulk carbonate $\delta^{13}C$ and $\delta^{18}O$ were analysed on oven-dried and pulverised sediment samples. Analyses were performed on a ThermoFisher Scientific 253plus gas isotope ratio mass spectrometer with a Kiel IV automated carbonate preparation device. Samples were treated with orthophosphoric acid at 75 °C. Analytical precision based on replicate analyses of in-house standard (Solnhofener Limestone) is of 0.03 ‰ and 0.04–0.06 ‰ (1σ) for $\delta^{13}C$ and $\delta^{18}O$, respectively. Data are reported relative to the Vienna Pee Dee Belemnite international standard, determined via adjustment to calibrated in-house standards.

Statistical analysis, Cluster and Detrended Correspondance Analysis (Suppl. Material S1), were carried out both in the bulk sediment and

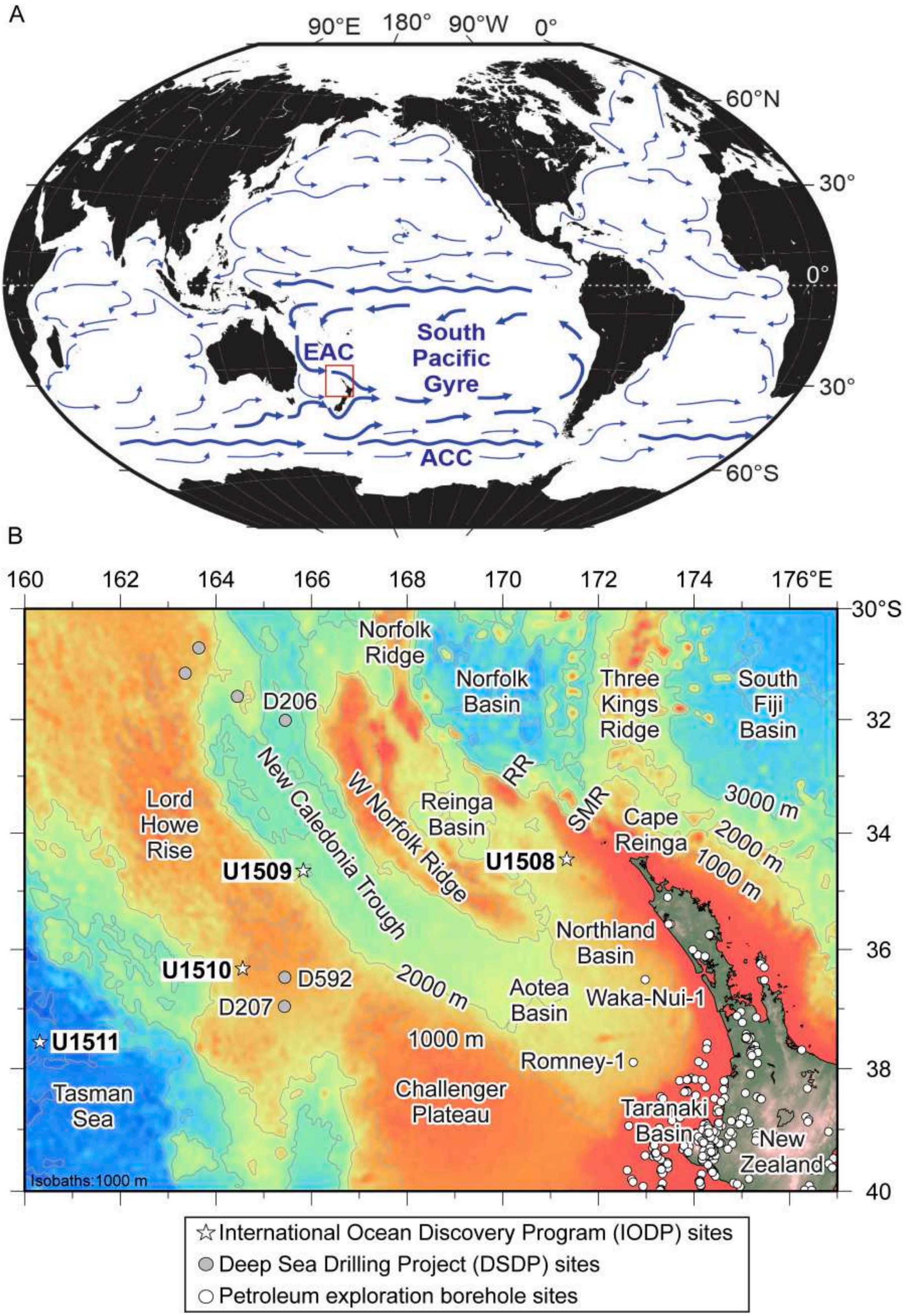

Fig. 1. Location of Site U1508. A. Global ocean currents affecting the region around Site U1508 (red box). EAC, Eastern Australian Current. ACC, Antarctic Circumpolar Current. B. Local bathymetric map showing the geographical names of the study area, including Reinga Ridge (RR) and South Maria Ridge (SMR), and the different drilled sites within it. (For interpretation of the references to colour in this figure legend, the reader is referred to the web version of this article.)

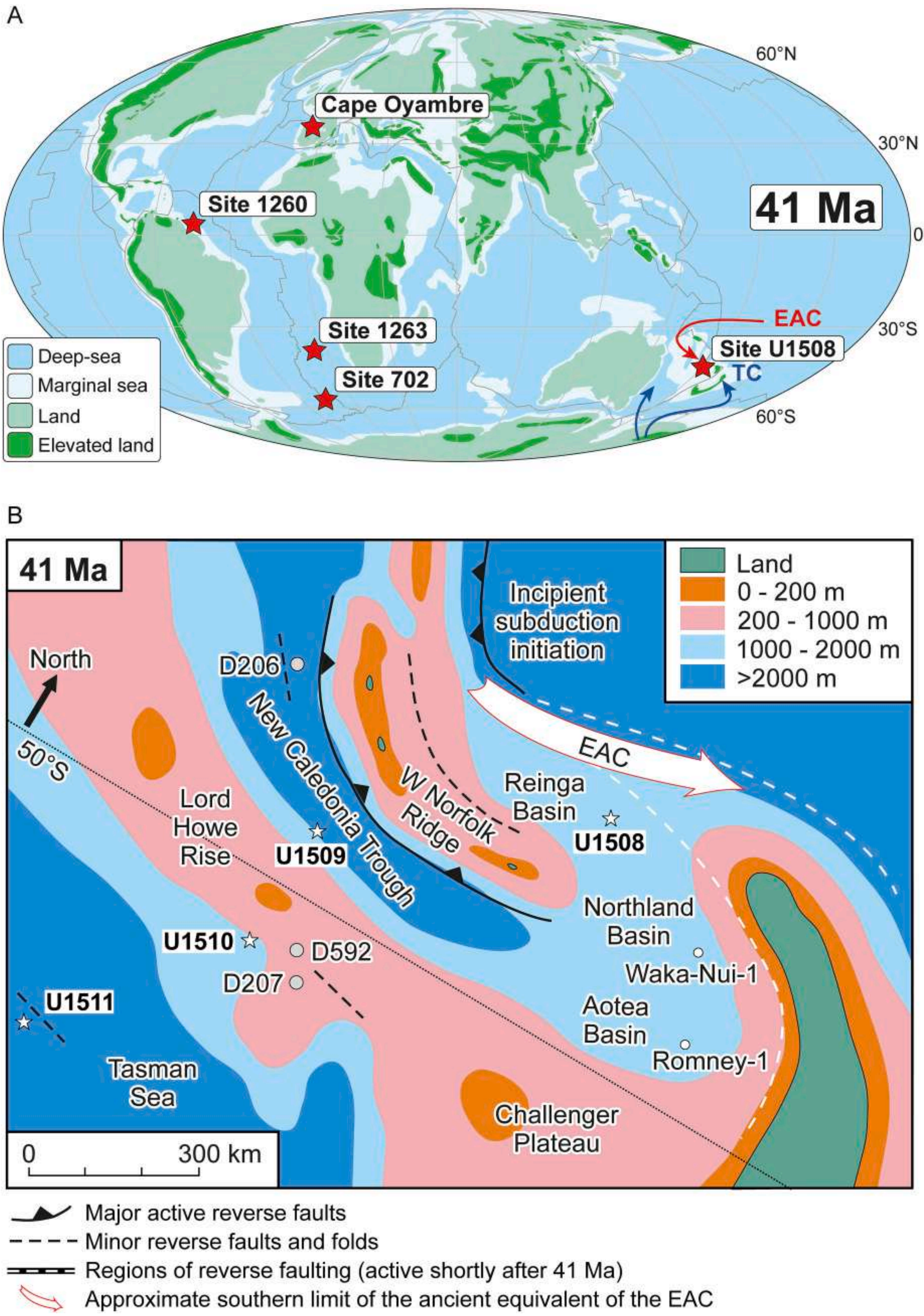

Fig. 2. A. Palaeogeographic maps at 41 Ma. A. Locations of sites where the LLTM has been studied. The blue arrows show the Tasman Current (TC), and the red one the Eastern Australian Current (EAC). Map drawn with GPlates (Müller et al., 2018). B. Local palaeogeography around Site U1508. Same symbols and area as in Fig. 1. (For interpretation of the references to colour in this figure legend, the reader is referred to the web version of this article.)

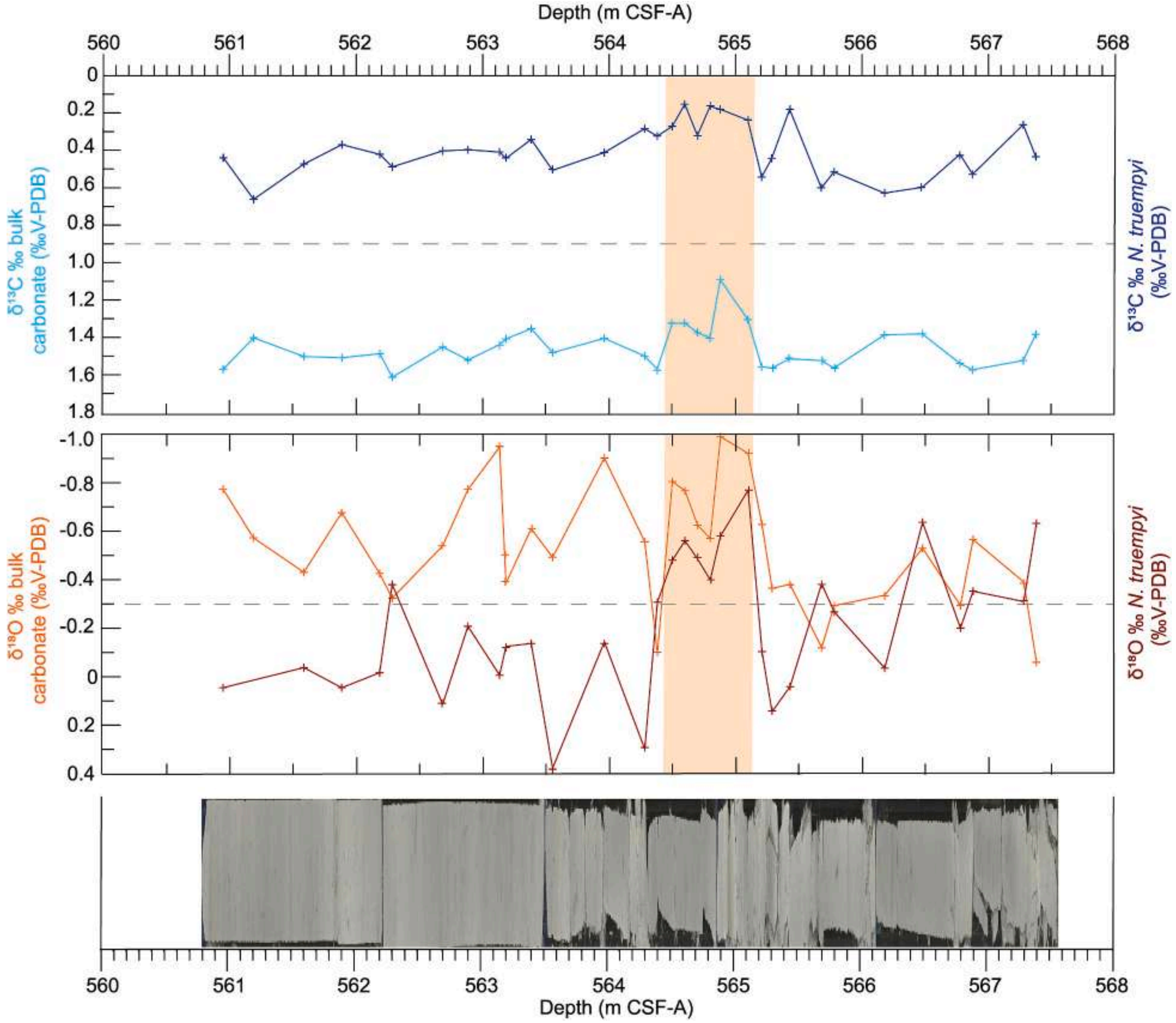

Fig. 3. Carbon and oxygen stable isotopes measured on bulk carbonate (lighter lines) and benthic foraminifera (*N. truempyi*, darker lines) from Core U1508C-22R, plotted against depth (m CSF-A). The orange box indicates the interval with the largest CIE and OIE.

benthic foraminifera carbon and oxygen stable isotopic records.

The $CaCO_3$ (%) (Fig. 6) content across the study interval includes the dataset of Bhattacharya (2021) between 564.03 and 566.19 m CSF-A, and calculated values based on shipboard Ca XRF data (560.82–567.45 m CSF-A; Sutherland et al., 2019), which were calibrated (Suppl. Table S1) using the results by Bhattacharya (2021).

3.2. *Organic geochemistry*

For organic geochemical analyses, 11 samples (20–30 g each, Suppl. Table S2) were freeze-dried and powdered prior to lipid extraction using microwave extraction (MEX) with 9:1 (v:v) dichloromethane:methanol (DCM:MeOH) as solvent. A known amount of a synthetic C46 glycerol trialkyl glycerol tetraether (GTGT) standard was added to the total lipid extract (TLE), which was separated into apolar, ketone, and polar fractions over an Al2O3 column with elution using hexane:DCM (9:1), hexane:DCM (1:1), and DCM:MeOH (1:1), respectively. The GDGT-containing polar fraction was subsequently dried and redissolved in hexane:isopropanol (99:1), and filtered over a 0.45 μm polytetrafluoroethylene filter to a concentration of ~3 mg mL–1, prior to analysis using ultrahigh-performance liquid chromatography–mass spectrometry (UHPLC-MS) on an Agilent 1260 Infinity series high-performance liquid chromatography system coupled to an Agilent 6130 single-quadrupole mass spectrometer in selected ion monitoring mode at Utrecht University, Utrecht, Netherlands. Chromatographic separation of target compounds was achieved on two Waters BEH HILIC silica columns (2.1 × 150 mm, 1.7 μm) preceded by a guard column (2.1 × 5 mm, Waters) packed with the same material. Solvents, elution scheme, and instrument settings were conducted according to Hopmans et al. (2004). Resulting chromatograms were integrated for the presence of isoprenoid GDGTs (isoGDGTs) and branched GDGTs (brGDGTs) (Schouten et al., 2013). GDGT distributions were calculated and analysed in line with recent Paleogene work covering a similar study area (Bijl et al., 2021).

3.3. *Magnetostratigraphy and global palaeogeography*

Shipboard palaeomagnetic analyses conducted in Hole U1508C during Exp. 371 are primarily based on quasi-continuous natural remanent magnetization (NRM) measurement of all archive halves (Suppl. Table S3). The initial NRM was measured every 5 cm before any treatment, and after each of four magnetic cleaning steps performed using alternate field (AF) of 10, 15, and 20 mT. The archive half measurements, conducted by using a *2G Enterprises* supercondicting rock magnetometer, were integrated with data from 29 oriented discrete specimens that were stepwise demagnetised up to 70 mT and measured after each demagnetization step with a *AGICO JR-6* spinner magnetometer (Sutherland et al., 2019). Because of the very low intensity of the NRM (~10^{-4} A/m), shipboard correlation of Hole U1508C with the geomagnetic polarity time scale (GPTS) was particularly difficult, and no palaeomagnetic reversals were retrieved in the upper Lutetian part of the site (~560–580 m CSF-A). To overcome this limitation, a total of 62 oriented 8 cm^3 cube-samples were trimmed from the working half of Cores 20R to 38R during the post-cruise sampling party. Samples were stepwise AF demagnetised up to a maximum field of 100 mT, using steps of 5 mT up to 50 mT and 10 mT up to the maximum value. Samples were measured automatically after each demagnetization step with a *2G Enterprises* superconducting rock magnetometer placed in line with the AF coil at the University of Bremen (Germany) (Mullender et al., 2016). Palaeomagnetic directions are determined after visual inspection of vector end-points demagnetization diagrams (Zijderveld, 1967). Vector end points linearly trending towards the origin of the demagnetization axes are interpolated by using principal component analysis as proposed by Kirschvink (1980). Vector end-points that fail to display a linear trend but show a coherent grouping in space are averaged by means of spherical statistic (Fisher, 1953).

The global palaeogeographic setting and the palaeoposition of the studied records are placed with respect the Earth's spin axis by using a palaeomagnetic reference frame. From the list compiled by Vaes et al. (2023), we selected a total of eight palaeomagnetic poles with an age ranging from 37 to 46 Ma (with an average of 40.73 Ma), five of which are from North America (Harlan et al., 1995; Irving et al., 2000; Symons et al., 2003; Ressetar and Martin, 1980; Sheriff and Shive, 1980), two from stable Europe (Dupont-Nivet et al., 2010; Hankard et al., 2007), and one from Greenland (Schmidt et al., 2005). The poles are first rotated into a common South African frame, depending on their age, by using the relative fits adopted by the relative plate motion model of Müller et al. (2016). The palaeo-position of the plates chained to South Africa at 41 Ma was then determined by using the same model after fixing the average palaeomagnetic pole as coinciding with the geographic pole. The main palaeo-elevation and palaeobathymetry features are drawn according to Cao et al. (2017).

3.4. Benthic foraminifera

Quantitative analyses of benthic foraminiferal assemblages were performed on the same 32 samples used for isotopic analyses (Suppl. Table S4). Sediment samples were oven dried at 40 °C, weighed and soaked in $Na_6(PO_3)_6$ over four hours. Disaggregated samples were then washed over a > 63 μm size fraction, and the remaining residue was oven-dried and weighed. Benthic foraminifera, with a moderate to poor preservation, are rare relative to total sediment particles in the >63 μm fraction of most studied samples. Additional sedimentary components include moderately well-preserved, dominant to abundant planktonic foraminifera and calcareous nannofossils, and a few poorly preserved radiolarians.

For the quantitative analyses, ca. 300 benthic foraminifera were picked per sample. Taxonomic classification mainly follows Alegret and Thomas (2001), Arreguín-Rodríguez et al. (2018), Hayward et al. (2010), Holbourn et al. (2013), Kaminski and Gradstein (2005), Loeblich Jr. and Tappan (1987) and Van Morkhoven et al. (1986). The specimens of the most representative species were photographed using the Scanning Electron Micrograph imaging facilities (JEOL JSM 6360-LV) at the Microscopy Service of the University of Zaragoza (Spain) (Figs. 7 to 9). A raw data matrix with the benthic foraminiferal counts (Suppl. Table S4) was used to calculate the relative abundance of each taxon; those whose relative abundance makes up >2 % of the assemblages in at least one sample are represented in Fig. 5. The percentage of calcareous and agglutinated tests, the planktonic/benthic foraminiferal ratio (P/B ratio, %; % planktonic relative to planktonic + benthic, e.g. Berger and Diester-Haass, 1988; Van der Zwaan et al., 1990), and diversity of benthic foraminiferal assemblages were calculated to describe changes in the assemblages and to infer the palaeoenvironmental conditions across the study interval (Fig. 6). The Shannon-Weaver heterogeneity index H (S) takes into account the number of species (S) and their relative abundance (p_i) in the sample (the proportion of the *i*th species, p = per cent divided by 100), and it was calculated following Murray (1991) and applying the formula H(S) $= -\Sigma\,(p_i.\ \ln p_i)$ in Excel. The Fisher-α diversity index was calculated using http://groundvegetationdb-web.com/ground_veg/home/diversity_index.The percentage of infaunal and epifaunal morphogroups (Corliss, 1991; Corliss and Chen, 1988; Jones and Charnock, 1985) was also calculated to infer trophic and oxygenation conditions in the deep sea (Fig. 6). Epifaunal morphogroups dominate the assemblages in oligotrophic, well-oxygenated environments, and infaunal taxa tend to be more abundant in eutrophic, oxygen-deficient conditions (Jorissen et al., 2007). Interpretations based on morphogroups must be taken carefully, considering that the relationship between morphology and habitat is sometimes problematic for living foraminifera (Buzas et al., 1993) and there are no perfect modern analogs for fossil assemblages (Hayward et al., 2012). This is particularly problematic if significant changes in the relative abundance of species of the same morphogroup end in a constant total abundance of that morphogroup (e.g. Alegret and Thomas, 2009; Alegret et al., 2021b).

The relative abundance of buliminids *s.l.* and the superfamily Buliminacea (Sen Gupta, 1999) was calculated (Fig. 6). These infaunal taxa are abundant in high food and/or low-oxygen conditions (Jorissen et al., 1995; Thomas, 1990), and their high abundance is most commonly related to a high food supply (Gooday, 2003; Jorissen et al., 1995, 2007).

Benthic foraminiferal accummulation rates (BFAR; Herguera and Berger, 1991), a proxy for total organic matter flux reaching the seafloor (Gooday, 2003; Herguera, 2000; Jorissen et al., 2007), were calculated by multiplying the number of benthic foraminifera per gram of bulk sediment by the linear sedimentation rate (derived from the refined age model) and the dry bulk sediment (Sutherland et al., 2019) (Fig. 6).

Benthic foraminiferal palaeobathymetric estimates are based on the comparison between recent and fossil assemblages, the occurrence and abundance of depth-related species, and their upper depth limits (e.g. Tjalsma and Lohmann, 1983; Van Morkhoven et al., 1986; Alegret and Thomas, 2001; Hayward et al., 2010; Gastaldello et al., 2024). We follow the bathymetric divisions by Van Morkhoven et al. (1986): neritic (0–200 m), upper bathyal (200–600 m), middle bathyal (600–1000 m), lower bathyal (1000–2000 m), and abyssal (>2000).

A qualitative analysis of the preservation of benthic foraminiferal tests was carried out across the study interval. Additionally, since planktonic foraminifera are more susceptible to fragmentation and dissolution than benthic foraminifera (Kucera et al., 1997), we calculated the planktonic foraminiferal fragmentation index (FI, Suppl. Table S4), following the method of Berger et al. (1982), to estimate changes in the carbonate saturation state of bottom waters (Berger et al., 1982; Kucera et al., 1997). At least 300 planktonic foraminiferal tests (complete and semi-complete tests), plus all the fragments (less than two-thirds of an entire test) were observed and counted in each sample. The number of fragments was divided by the total number of tests, and multiplied by 100. Assemblages with FI values higher than 40% are correlated with strong dissolution (Kucera et al., 1997; Gilabert et al., 2021).

4. Results

4.1. Inorganic geochemistry

In Core U1508C-22R, bulk carbonate $\delta^{13}C$ ($\delta^{13}C_{bulk}$) values range from 1.09‰ to 1.61‰ (mean value 1.45‰), and bulk carbonate $\delta^{18}O$ ($\delta^{18}O_{bulk}$) ranges from −0.99 ‰ to −0.06 ‰ (average value of −0.54‰). Three intervals are differentiated based on the $\delta^{13}C$ and $\delta^{18}O$ records

(Fig. 3). The delineation of the three intervals and the identification of the LLTM event is also supported by a Cluster Analysis and a Detrended Correspondance Analysis (DCA; Suppl. Material S1).

The lowermost part of the study section (Interval 1, from 567.40 to 565.15 m CSF-A) shows $\delta^{13}C_{bulk}$ values higher than 1.38 ‰ (average of 1.50‰), and $\delta^{18}O_{bulk}$ values higher than −0.63 ‰ (average of 0.36 ‰). Interval 2 (between 565.15 and 564.45 m CSF-A) is characterised by the largest negative CIE and OIE; $\delta^{13}C_{bulk}$ values (average of 1.30 ‰) show a negative shift of 0.47 ‰ (decrease from 1.56 ‰ at 565.22 m CSF-A to 1.09 ‰ at 564.9 m CSF-A), and $\delta^{18}O_{bulk}$ values (average of −0.78 ‰) show a negative shift of 0.45 ‰ (decrease from an average of −0.36 ‰ in the previous interval to −0.99 ‰ at 564.9 m CSF-A). In the uppermost interval (Interval 3, from 564.45 to 560.96 m CSF-A), $\delta^{13}C_{bulk}$ values are higher than 1.35 ‰, with an average of 1.48 ‰, and $\delta^{18}O_{bulk}$ values are higher than −0.7 ‰ with an average of −0.57 ‰.

The isotope values measured on the epifaunal species *Nuttallides truempyi* show a similar trend compared to bulk isotope values (Fig. 3). Mono-specific $\delta^{13}C_{benthic}$ values range between 0.15 ‰ and 0.63 ‰ (average 0.4 ‰), and $\delta^{18}O_{benthic}$ values range between −0.83 ‰ and 0.38 ‰ (average − 0.23 ‰). Interval 1 shows $\delta^{13}C_{benthic}$ values higher than 0.25 ‰ (average of 0.47 ‰), and $\delta^{18}O_{benthic}$ values are higher than −0.3 ‰ (average of −0.25 ‰). Within Interval 2, $\delta^{13}C_{benthic}$ values range from 0.54 ‰ to 0.18 ‰ at 564.9 m CSF-A (CIE 0.36 ‰, interval average of 0.22 ‰), whereas $\delta^{18}O_{benthic}$ values decrease from −0.1 to −0.58 ‰ (OIE 0.48 ‰, interval average of −0.55 ‰). In Interval 3, $\delta^{13}C_{benthic}$ values are higher than 0.28 ‰ (average 0.44 ‰) and $\delta^{18}O_{benthic}$ values are higher than −0.38 ‰ (average − 0.09 ‰).

The percentage of $CaCO_3$ derived from the Ca XRF data ranges between 67.85 % (565.41 m CSF-A) and 87.55 % (561.98 m CSF-A), with an average of 83.92 % (Fig. 6). The $CaCO_3$ content (%) decreases by ~15 % between 565.41 and 564.89 m CSF-A, with an average of 74.65 %. A lower-resolution study by Bhattacharya (2021) reported a similar drop of 11 % in the $CaCO_3$ content across this interval (Fig. 6).

4.2. Organic geochemistry

The 11 samples from Hole U1508C (Fig. 6) contain appropriate concentrations for GDGT analyses. However, several indicator ratios are elevated and record an influence of non-normal marine GDGT distributions. In particular, BIT indices are relatively high, ranging between 0.32 and 0.72 (average 0.54), suggesting terrestrial input of GDGTs. Moreover, indicator ratios within the isoGDGT pool are likewise elevated above their suggested thresholds. These include a high Methane Index (MI; Zhang et al., 2011) that is near or above the suggested threshold of 0.3 throughout the studied section and a high AOM ratio (GDGT-2/Crenarcheol; Weijers et al., 2011) consistenly at or above the suggested threshold of 0.2. These ratios indicate a contribution to the GDGT pool by methane-metabolizing archaea and anaerobic methane oxidizers, respectively. The GDGT-2/3 ratio (Taylor et al., 2013) is higher than 5 in all samples, also suggesting a contribution of deep-dwelling archaea. Maximum values of all of these indicator ratios are found in stratigraphic Interval 2. TEX_{86} values range quite widely between 0.34 and 0.72. However, the combination of all indicator ratios with values outside the normal range indicates TEX_{86} should not simply be used as a temperature proxy in this specific interval and location, as the composition of GDGTs used in the index is too heavily influenced by non-thermal contributions.

4.3. Magnetostratigraphy

From the total of 62 samples collected from Hole U1508C, a characteristic remanent magnetization (ChRM) that is suitable for magnetic polarity stratigraphy was isolated in 32 samples (i.e., ~52 %). Overall, the low intensity of the NRM resulted in a relatively poor preservation of the palaeomagnetic signal, and the ChRM directions possessing a maximum angular deviation (MAD, which express the angular uncertainty associated to the direction) lower than 10° is 13. A maximum MAD of 10° is often considered as a limit of acceptability for ChRM directions used for palaeolatitude estimates, which require precise data (Dallanave et al., 2022), nonetheless directions with higher confidence angle can be used for magnetic polarity interpretation. After integration with 12 palaeomagnetic directions derived from the shipboard analysis, we found at Hole U1508C (Cores 20R to 38R) seven polarity zones that correlate continuously with Chrons C18r – C21r (Dallanave and Chang, 2020). In particular, a total of 12 palaeomagnetic directions have been obtained within Cores 22R and 24R (Suppl. Table S3, Fig. S1). Within this chronological frame, the reversed polarity interval within 562.62 m and 580.01 m CSF-A (Cores 22R–24R) is correlated with Chron C19r (Suppl. Fig. S1).

4.4. Age model and identification of the LLTM

The available age model for Site U1508 (Sutherland et al., 2019) was refined using magneto- and biostratigraphic (calcareous nannofossil) data, and the new age model indicates that Core U1508C-22R spans the LLTM event (Fig. 4; Suppl. Table S6). Previously studied successions evidenced that the LLTM lies within Chron C19r (Edgar et al., 2007; Westerhold et al., 2018), which is documented at Site U1508 from 565.11 to 564.51 m CSF-A (Dallanave and Chang, 2020). Using the chron ages of Westerhold et al. (2020), their relative depths (Sutherland et al., 2019; Dallanave and Chang, 2020), calcareous nannofossil datums, and assuming constant linear sedimentation rates between two successive chron boundaries, we constructed an age-depth plot for Site U1508 (Fig. 4).

According to this new age model (Fig. 4), the study interval spans calcareous nannofossil Eocene biozones CNE13 and CNE14 (Agnini et al., 2014), whose boundary is marked by the Base of Common (and continuous) of *C. reticulatum*. Assuming linear sedimentation rates between successive tie points, an age (Ma) was calculated for each study sample (Suppl. Table S6).

The interval containing the $\delta^{13}C$ and $\delta^{18}O$ negative excursions (Fig. 3) in Hole U1508C is correlated with the LLTM event based on its position in the upper part of Chron C19r (Fig. 4), with an estimated duration of 30 kyr (41.39–41.36 Ma). This is consistent with the duration and age of the LLTM CIE calibrated in the Atlantic Ocean (41.52 Ma; Westerhold et al., 2018). The small discrepancy in the age of the event is possibly linked to the assumption of a constant accumulation rate within the chron, while the calibration by Westerhold et al. (2018) is based on a more refined astronomical tuning.

4.5. Planktonic foraminiferal fragmentation index (FI)

The calculated FI values at Site U1508 (Fig. 6) range from 0.62 % to 8.64 %. In Interval 1, FI values average 1.31 %, and the maximum value of 3.22 % is recorded at 565.3 m CSF-A. Values are higher than 3.5 % in Interval 2, with an average of 5.88 % and a maximum value of 8.64 % at 564.4 m CSF-A, and a qualitative analysis of planktonic foraminifera reveals a poorer preservation of their tests. The FI decreases in Interval 3, with an average value of 2.43 %.

4.6. Benthic foraminiferal assemblages

A total of 65 taxa (53 calcareous and 12 agglutinated) were recognised at the species or higher taxonomic level. Benthic foraminiferal assemblages are strongly dominated by calcareous taxa (≥80 % of the assemblages) across the study interval, and agglutinated foraminifera are a minor component (Fig. 6) and mostly consist of infaunal biserial-triserial species such as *Spiroplectammina spectabilis* or *Karreriella bradyi* (Fig. 5).

Infaunal morphogrups make up 58 % - 73.25 % of the assemblages, and they also dominate among calcareous hyaline foraminifera (Fig. 6). They include common to abundant uniserial elongated nodosariids and

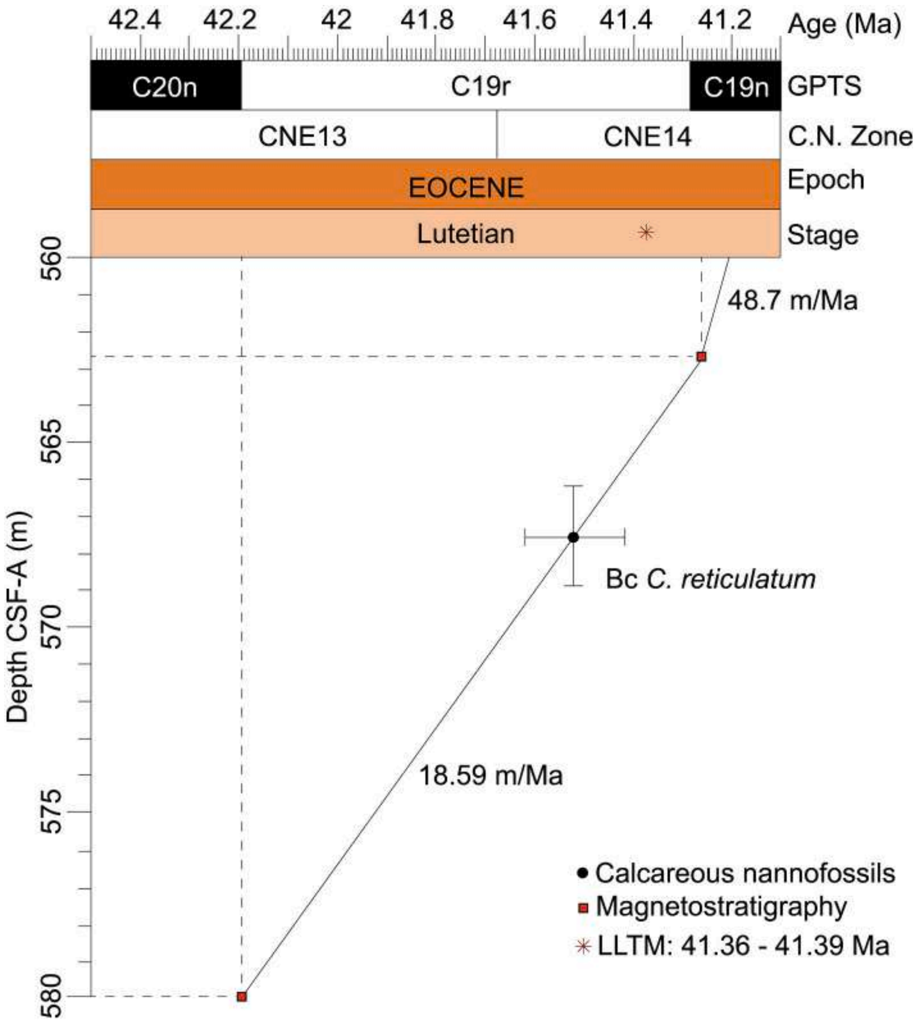

Fig. 4. Refined age model for IODP Hole U1508C. Magnetostratigraphy data from Dallanave and Chang (2020). Age data from Westerhold et al. (2020). Depth CSF-A (m) data from Sutherland et al. (2019). Bc *C. reticulatum* (Base of Zone CNE14) from Agnini et al. (2014).

stilostomellids, and biserial species sush as *Pleurostomella* and *Uvigerina peregrina*, triserial buliminids *s.l.*, globular unilocular tests (e.g., *Lagena*) and subglobular species (*Globocassidulina subglobosa*), planispiral biconvex taxa such as *Lenticulina* spp., and the trochospiral *Oridorsalis umbonatus*. Among epifaunal morphogroups, *Nuttallides truempyi, Gyroidinoides* spp. and *Cibicidoides* spp. (incl. *C. praemundulus*) are the most common taxa (Fig. 6).

The assemblages are moderately diverse throughout the study interval. The Fisher-α diversity index ranges between 10.60 and 17.30 (average 13.12). The heterogeneity H(S) index, with an average of 2.88, ranges from a minimum of 2.61 to a maximum of 3.08. BFAR values, with an average of 632.91, range between 1409.27 and 209.97 specimens/cm^2*kyr, and the P/B ratio, with an average of 93 %, remains high across the study interval (between 87 % and 98 %). All these indices reach their minimum values in Interval 2, coinciding with the negative CIE that marks the LLTM (Fig. 6). No extinctions of benthic foraminifera have been recorded across the study interval, but assemblages show changes in diversity and in the relative abundance of taxa.

Interval 1 (567.4–565.15 m CSF-A, 41.52–41.40 Ma) is characterised by the dominance of infaunal calcareous taxa (Fig. 6), mainly *G. subglobosa*, *Pyrimidina* sp. and *Lenticulina* spp., and the calcareous epifaunal species *C. praemundulus* and *N. truempyi* are abundant (Fig. 5). *Alabamina dissonata* is common across this interval. Diversity (Fisher-α average = 12.74) and heterogeneity of the assemblages (average of 2.9), and the percentage of *G. subglobosa* and *Pyramidina* sp. show a positive peak in the middle of the interval, progressively decreasing from 566 m CSF-A towards the top of Interval 1. BFAR values (average of 826.85 specimens/cm^2*kyr) range between 361.37 and 1409.2 specimens/cm^2*kyr. The percentage of $CaCO_3$ decreases from the middle towards the top of Interval 1, where the lowest value is recorded (at 565.21 m CSF-A). A slight decrease in the P/B ratio (from∼ 92 % to∼ 87 %) is observed at the top of this interval.

Interval 2 (565.15–564.45 m CSF-A, 41.40–41.36 Ma) is characterised by an increase in the relative abundance of some infaunal taxa such as bi-triserial agglutinated foraminifera, *Lenticulina* spp., *Uvigerina peregrina, Oridorsalis umbonatus*, *Turrillina brevispira* and the superfamily Buliminacea (incl. *Bulimina tuxpamensis*) (Fig. 5). The relative abundance of the epifaunal species *C. praemundulus* peaks within this interval, gradually declining thereafter from its midpoint. The species *A. dissonata*, *G. subglobosa* and *Pullenia bulloides* decrease in abundance as compared to Interval 1. Benthic assemblages show the lowest diversity and heterogeneity values, and the lowest P/B ratio has also been recorded (Fig. 6). BFARs are low, and show their minimum value in the middle of this interval. The lower part of this interval shows $CaCO_3$ values around 70 %, and they progressively increase back to levels comparable to those observed in the lower part of Interval 1. Calcareous taxa clearly dominate the assemblages, but two minimum values (84 % and 80 %) have been recorded at 565.11 m and 564.8 m, respectively (Fig. 6).

Interval 3 (564.45–560.96 m CSF-A, 41.36–41.23 Ma) is

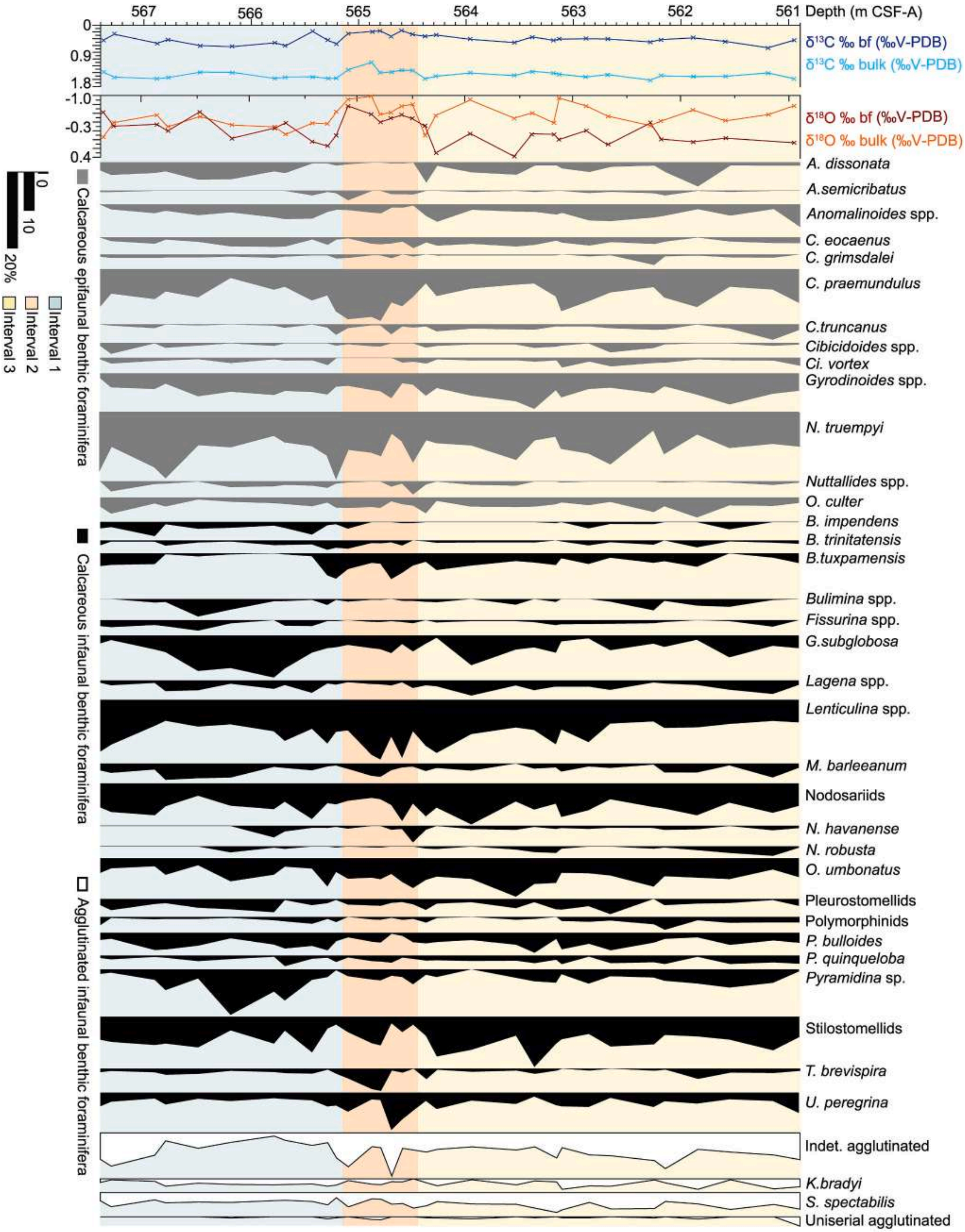

Fig. 5. Carbon and oxygen stable isotopes (measured on bulk carbonate and benthic foraminifera) across IODP Core U1508C-22R, and relative abundance of benthic foraminiferal taxa that make up >2% of the assemblages, plotted against depth (m CSF-A).

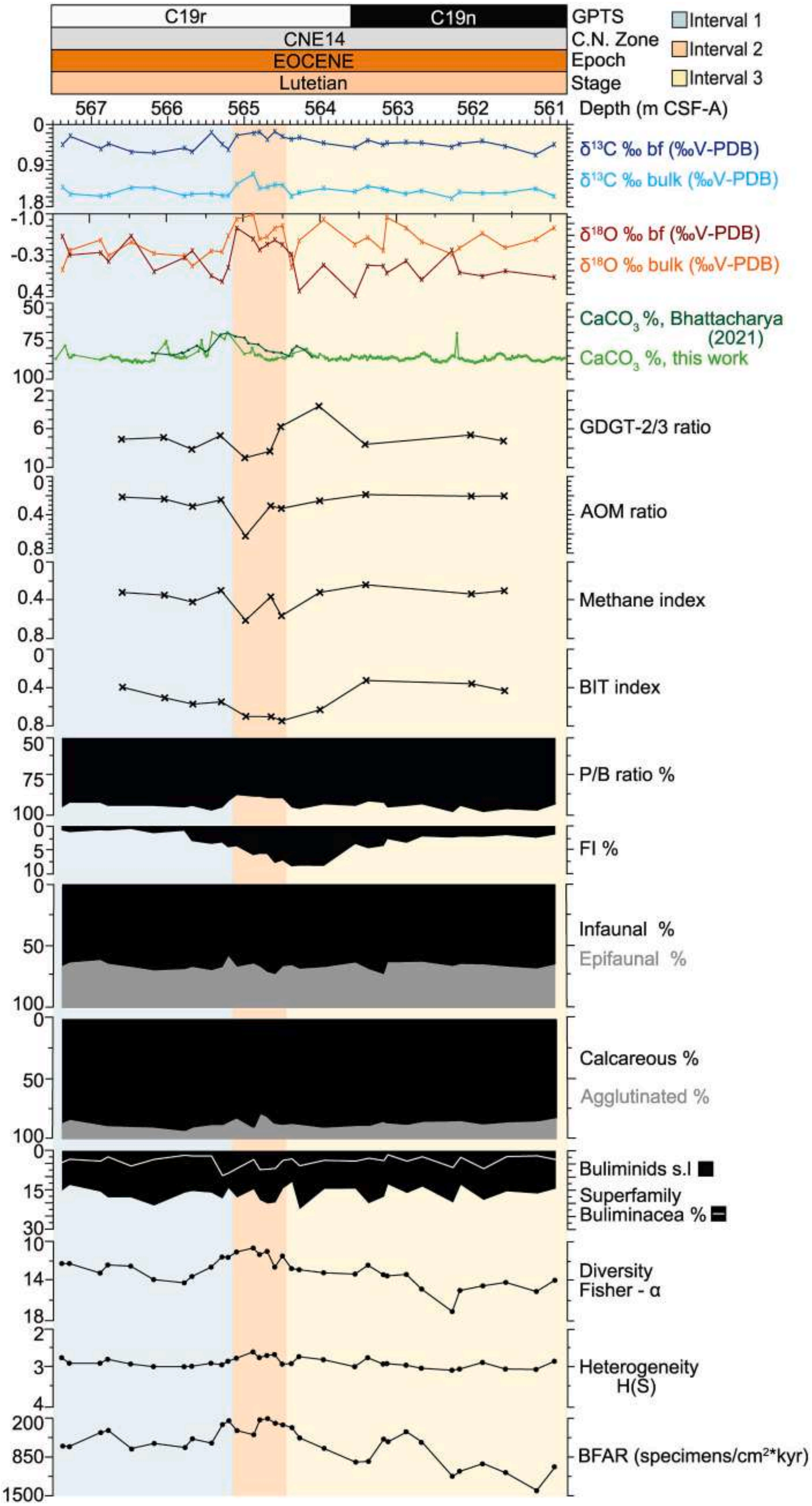

Fig. 6. Geochemical and faunal indices across the study interval at IODP Site U1508, plotted against depth (m CSF-A): carbon and oxygen stable isotopes, $CaCO_3$%, organic geochemistry (GDGT-2/3ratio (GDGT-2/GDGT-3), AOM ratio (GDGT-2/Cren), Methane index and BIT index), planktonic/benthic foraminifera (P/B) ratio, fragmentation index (FI) of planktonic foraminifera, benthic foraminiferal groups and diversity indices, benthic foraminiferal accummulation rates (BFAR).

characterised by the dominance of calcareous infaunal foraminifera, mainly stilostomellids, nodosariids, *O. umbonatus*, and *Lenticulina* spp. Infaunal biserial-triserial agglutinated groups are also common. Among epifaunal taxa, *N. truempyi, C. praemundulus* and *Gyroidinoides* spp. are most abundant, and *A. dissonata* becomes a common component of the assemblages, as in Interval 1. Diversity and heterogeneity of the assemblages increase upwards. The P/B ratio is higher than in Interval 2, and BFAR values significantly increase upwards, showing the highest absolute values in the upper part of Interval 3. The $CaCO_3$ values average 84 % and are pretty constant throughout Interval 3, apart from a minor (6 %) decrease in its lower part. The species *G. subglobosa* is slightly more abundant than in Interval 2, but it does not reach the numbers observed in the middle of Interval 1.

A qualitative analysis of the benthic foraminiferal preservation reveals that the intervals between 560.96 and 563.15 m CSF-A (upper half of Interval 3) and 565.7–567.4 m CSF-A (most part of Interval 1) are characterised by moderately preserved tests and a higher number of complete stilostomellids and nodosariids. In contrast, a poorer preservation of the tests has been observed between 563.2 and 565.45 m CSF-A, from the uppermost part of Interval 1 to the lower half of Interval 3 (e.g. Fig. 7, photographs 3, 7, 10; Fig. 8, photographs 1, 3, 4; Fig. 9, photograph 11), with stilostomellids and nodosariids commonly broken.

5. Interpretation and discussion

5.1. Palaeobathymetry

Shipboard data of benthic microfossils (foraminifera and ostracods) for Site U1508 suggest a lower bathyal depth of deposition during the Paleocene and early-middle Eocene, and slightly shallower palaeodepths (deep middle bathyal) during late Eocene and the Oligocene (Sutherland et al., 2019).

Focusing on the Lutetian interval at this site, the most abundant benthic foraminiferal species such as *Cibicidoides praemundulus, Nuttallides truempyi, Oridorsalis umbonatus* and *Globocassidulina subglobosa* are typical of lower bathyal to abyssal depths (Van Morkhoven et al., 1986; Hayward et al., 2001, 2004, 2010). A similar palaeodepth has been assigned for the less abundant *Nonion havanense* (Tjalsma and Lohmann, 1983; Bignot, 1998; Katz et al., 2003) and *Pleurostomella* (Hayward et al., 2001). *Stilostomella* and *Uvigerina peregrina* are common at Site U1508, and they occur predominantly at lower bathyal to upper abyssal depths between 1000 and 3000 m (Pflum and Frerichs, 1976; Mead, 1985). Species with an upper depth limit at 1000–1500 m, such as *Alabamina dissonata* and *Cibicidoides grimsdalei* (Van Morkhoven et al., 1986), have been identified. These data, combined with the low abundance of *A. dissonata*, which was rare above 2 km during the Eocene (Van Morkhoven et al., 1986), suggest a lower bathyal depth of deposition during the Lutetian at Site U1508, consistent with the shipboard data (Sutherland et al., 2019).

5.2. Palaeoenvironmental interpretation across the LLTM at IODP Site U1508

Carbon and oxygen stable isotope records in bulk sediment and benthic foraminifera show negative shifts that denote Interval 2 (41.40–41.36 Ma), which corresponds to the LLTM according to our refined age model. The lack of the expected surface-to-deep vertical gradient in oxygen isotopes, especially in Intervals 1 (41.52–41.40 Ma) and 2 and in isolated samples from the base and upper half of Interval 3 (41.36–41.23 Ma), indicates that the oxygen isotopic signal has been likely overprinted by diagenesis. The vertical gradient can be observed in carbon isotopes, and we confidently used the paired negative shift in $\delta^{13}C_{bulk}$ and $\delta^{13}C_{benthic}$ values to identify a Lutetian hyperthermal event (Figs. 3, 10).

In terms of organic geochemistry, several indices (BIT, MI, AOM index, GDGT-2/3) record elevated values, with peak values being reached in Interval 2. While this makes the GDGT assemblage unsuitable for TEX_{86}-based palaeothermometry, the turnover in the GDGT assemblage is by itself reflective of a change in the GDGT-producing microbial community. Specifically, the increase in GDGT-2/3 indicates a deepening of the source of the sedimentary GDGT signal, i.e. an increased contribution of deep-dwelling archaea relative to surface-dwellers (Taylor et al., 2013, see also discussion in van der Weijst et al., 2022). We surmise this deepening of the signal might relate to a shallowing of the thermocline, causing enhanced relative contribution of sub-thermocline GDGT-producers to the sedimentary pool. Increased thermal stratification and shallowing of the thermocline is the expected oceanographic response to global warming (Gruber, 2011), in this case the probable LLTM warming (Figs. 6, 10).

Benthic foraminiferal assemblages are dominated by calcareous taxa (Figs. 6, 10), indicating deposition above the carbonate compensation depth. Infaunal morphogroups are more abundant (average of 66.7 %) than epifaunal ones (average of 33.3 %) (Figs. 6, 10) and point to meso-oligotrophic conditions. This interpretation is supported by the common occurrence of the oligotrophic species *N. truempyi* (Thomas et al., 2000; Arreguín-Rodríguez and Alegret, 2016; Rivero-Cuesta et al., 2020), and the low relative abundance of the superfamily Buliminacea (average 4.2 % of the assemblages) and buliminids *s.l.* (average 16.5 %) (Fig. 10), which in the modern oceans are most common at sites with an abundant food supply (e.g., Fontanier et al., 2002).

A slight decrease in diversity of the assemblages towards the top of Interval 1 likely indicates environmental stress at the seafloor prior to the LLTM (Interval 2) (Fig. 10). The decrease in diversity was mostly driven by a moderate increase in the percentage of *N. truempyi, B. tuxpamensis, C. praemundulus* and agglutinated biserial-triserial species (Figs. 5, 10). The first species is an oligotrophic taxon that thrived in carbonate-corrosive bottom waters during the ealiest Eocene (Alegret and Thomas, 2009, Alegret et al., 2018, Alegret et al., 2021a). This species, however, only makes up to 16.8 % of the assemblages at Site U1508. *Bulimina tuxpamensis* increased in abundance after the PETM at several sites in the Atlantic Ocean (Alegret and Thomas, 2009, Alegret et al., 2018; D'haenens et al., 2012) and also survived the PETM extinction in the Pacific Ocean (Takeda and Kaiho, 2007; Kawahata et al., 2015), and *C. praemundulus* has been interpreted as a resilient species across the LLTM in the Atlantic Ocean (Rivero-Cuesta et al., 2020). These data point to environmental stress towards the uppermost part of Interval 1, likely due to the early signals of the LLTM. The moderate decrease in BFAR (Fig. 10) is interpreted as a slight decrease in export productivity, which is consistent with the increase in the oligotrophic species *N. truempyi*. The $CaCO_3$% and the P/B ratio slightly decrease towards the uppermost part of Interval 1, but the assemblages are dominated by calcareous taxa (average of 90.3 %), and although the FI shows a minor increase (up to 4.6 %), it still shows very low values and does not reach the values associated with strong dissolution (40 %; Kucera et al., 1997) (Figs. 6, 10). We suggest these changes might be indicative of a slight increase in $CaCO_3$-corrosivity of bottom waters, but no significant dissolution.

The base of Interval 2 is defined by the negative CIE and OIE that mark the onset of the LLTM. The lack of vertical isotope gradient in $\delta^{18}O_{bulk}$ and $\delta^{18}O_{benthic}$ values indicates these may have been overprinted by diagenesis, and although they have not been used to infer palaeotemperatures, we suggest they are associated with warming of surface and bottom waters during the LLTM. This interpretation is consistent with results of organic geochemistry analyses, which indicate a shallowing of the thermocline linked to increased stratification in the water column.

No extinctions of benthic foraminifera have been recorded across the LLTM at Site U1508, but diversity and heterogeneity of the assemblages keep decreasing across the lower half of the LLTM Interval 2 (Fig. 10). Interval 2 is also characterised by the high abundance of *C. praemundulus* (interpreted as a resilient species across the LLTM in the Atlantic Ocean; Rivero-Cuesta et al., 2020), and the dysoxic genus *Lenticulina* (Lohmann,

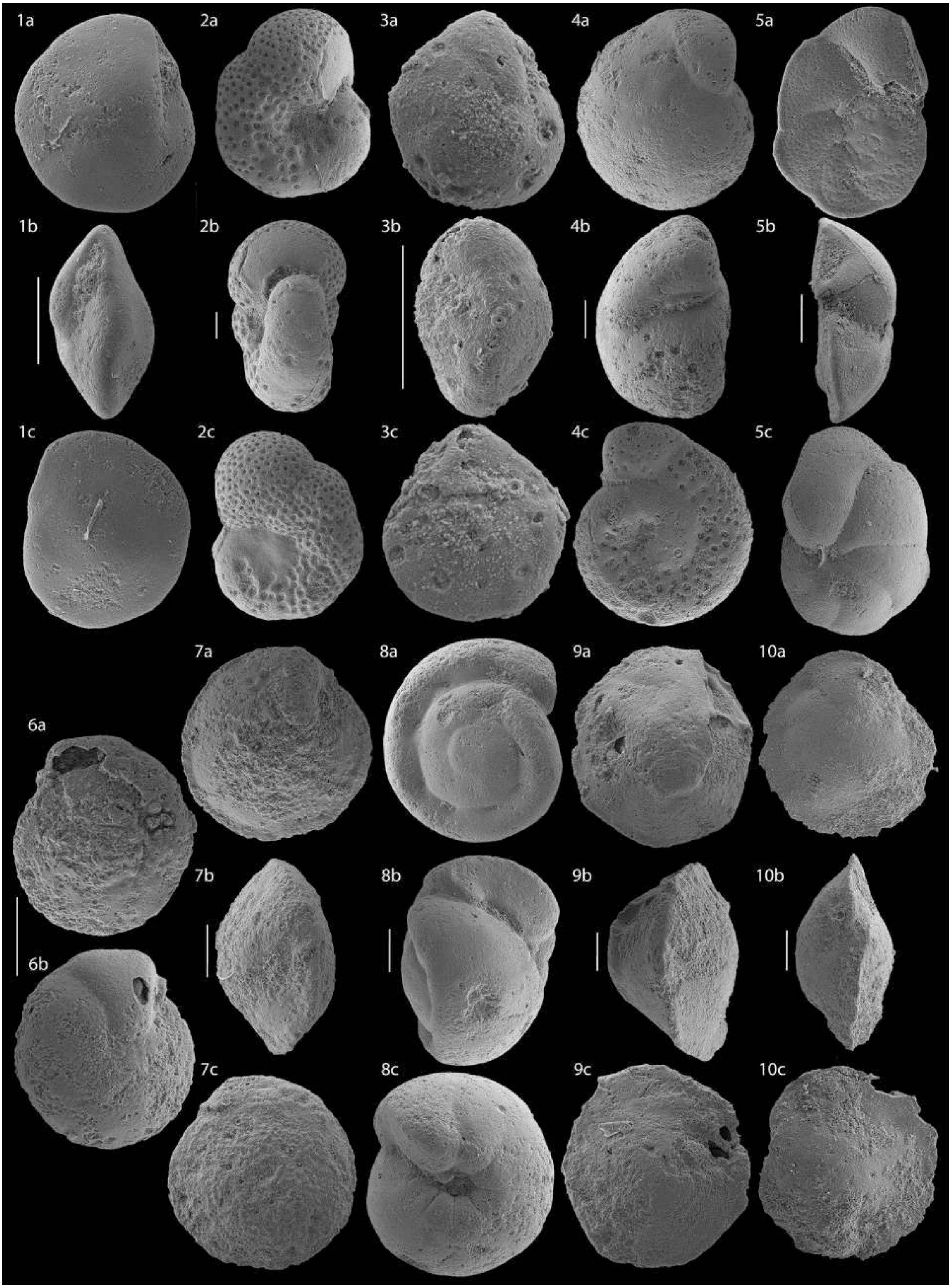

Fig. 7. SEM images of the most common benthic foraminiferal taxa across the study interval. 1a-c: *Alabamina dissonata,* sample U1508C, 22R (4, 84–85 cm); 2a-c: *Anomalinoides semicribatus*, sample U1508C, 22R (1, 137–138 cm); 3a-c: *Cibicidoides eocaenus,* sample U1508C, 22R (3, 89–90 cm); 4a-c: *Cibicidoides grimsdalei,* sample U1508C, 22R (2, 45–47 cm); 5a-c: *Cibicides vortex,* sample U1508C, 22R (5, 5–7 cm); 6a-b: *Cibicidoides praemundulus,* sample U1508C, 22R (1, 15–16 cm); 7a-c: *Cibicidoides truncanus,* sample U1508C, 22R (2, 119-120 cm); 8a-c*: Gyroidinoides* sp., sample U1508C, 22R (1, 15–16 cm); 9a-c: *Nuttallides truempyi,* sample U1508C, 22R (4, 84–85 cm); 10 a-c: *Osangularia culter,* sample U1508C, 22R (3, 89–90 cm). All scale bars = 100 μm.

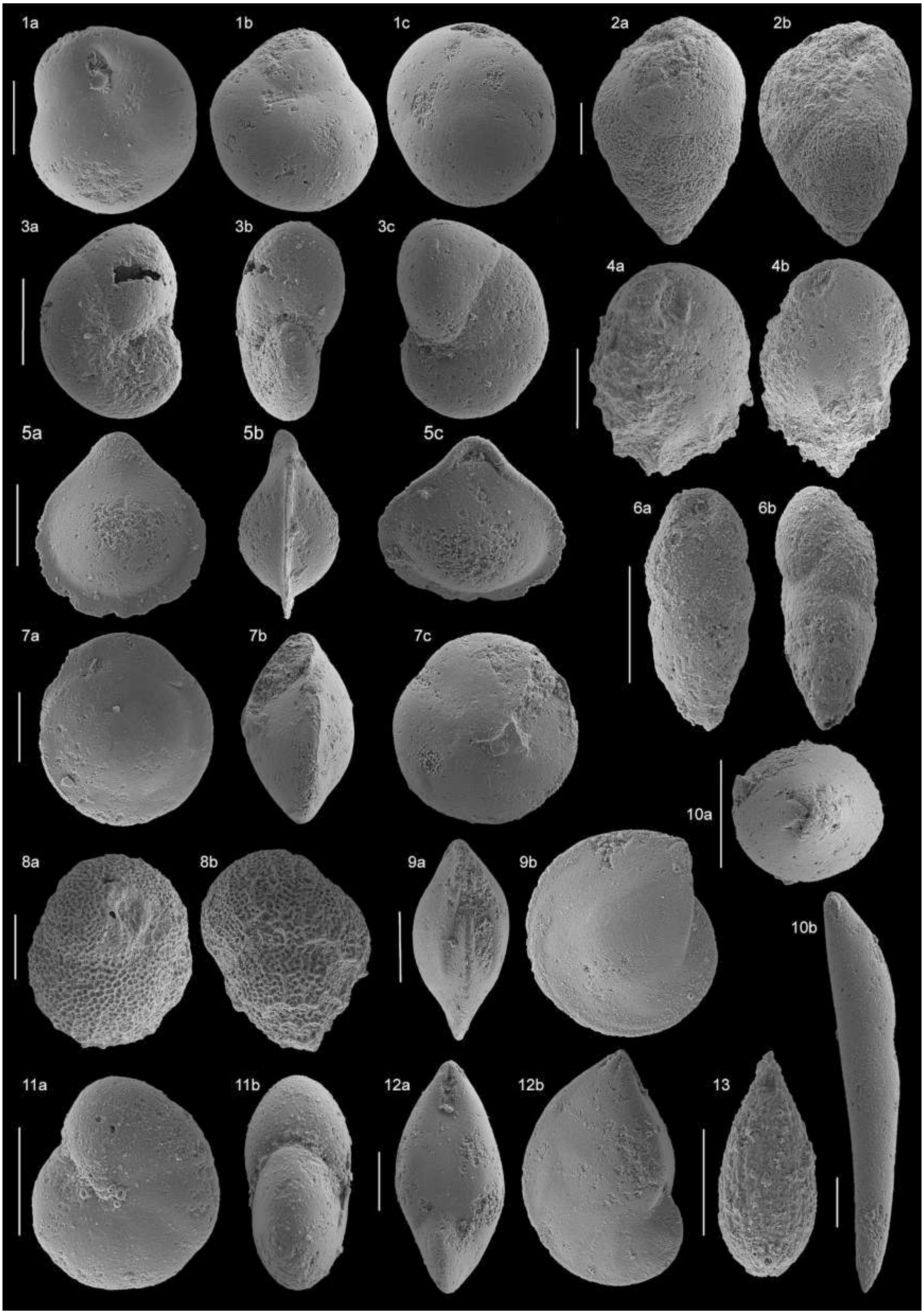

Fig. 8. SEM images of the most common benthic foraminiferal taxa across the study interval. 1a-c: *Globocassidulina subglobosa,* sample U1508C, 22R (3, 46–47 cm); 2a-b: *Bulimina tuxpamensis,* sample U1508C, 22R (2, 5–6 cm); 3a-c: *Nonionella robusta,* sample U1508C, 22R (3, 79–80 cm); 4a-b: *Bulimina trinitatensis,* sample U1508C, 22R (4, 6–7 cm); 5a-c: *Fissurina fimbriata,* sample U1508C, 22R (3, 5–6 cm); 6a-c: *Bulimina thanetensis,* sample U1508C, 22R (3, 89–90 cm); 7a-c: *Oridorsalis umbonatus,* sample U1508C, 22R (5, 5–7 cm); 8 a-b: *Bulimina impendens,* sample U1508C, 22R (2, 67–69 cm); 9a-b: *Lenticulina* sp. 1, sample U1508C, 22R (4, 84–85 cm); 10 a-b: Nodosariid, sample U1508C, 22R (2, 91–92 cm); 11 a-b: *Nonion havanense,* sample U1508C, 22R (3, 89–90 cm)*;* 12a-b: *Lenticulina* sp. 2*,* sample U1508C, 22R (3, 100–101.5 cm); 13: *Lagena* sp., sample U1508C, 22R (3, 46–47 cm). All scale bars = 100 μm.

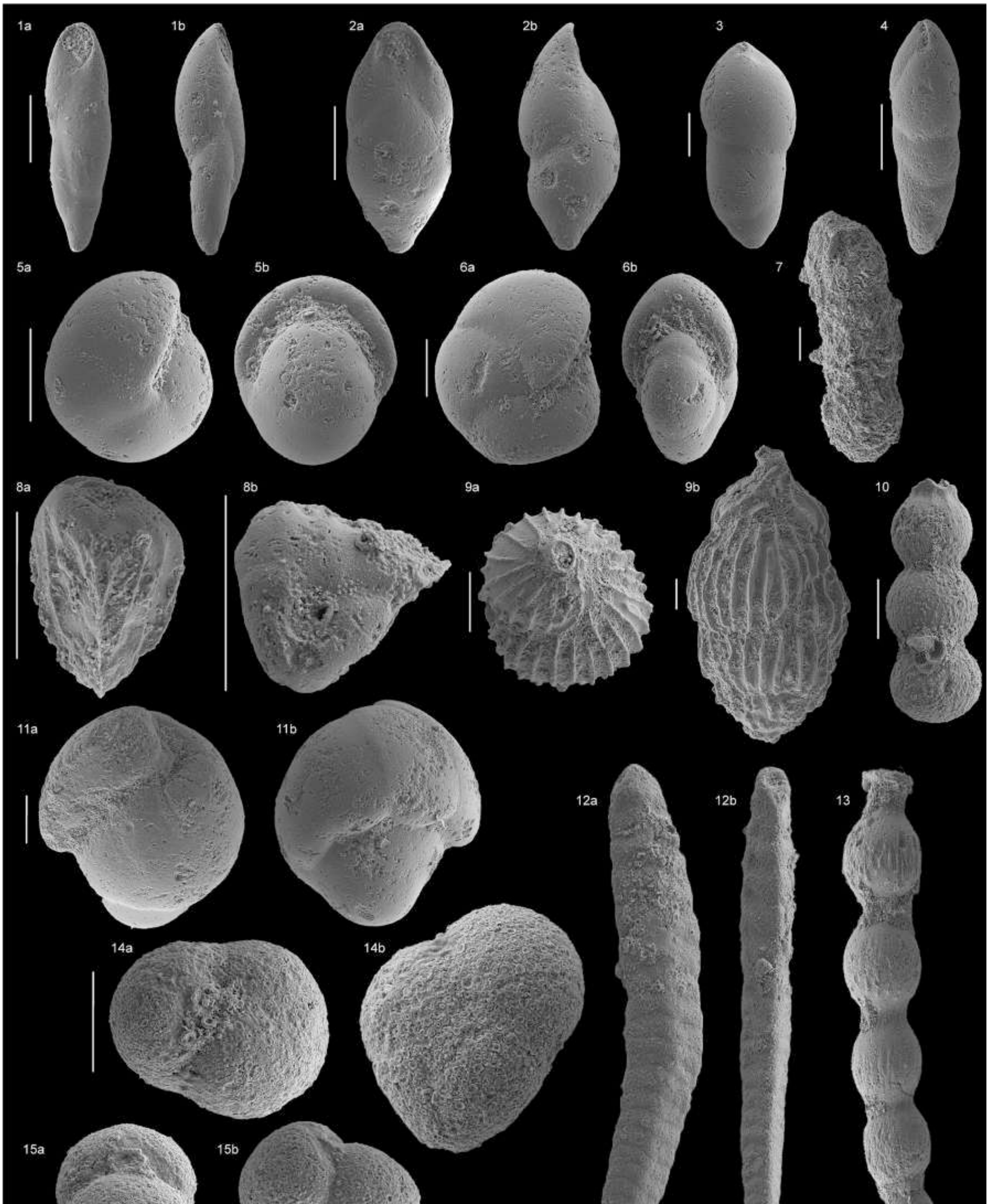

Fig. 9. SEM images of the most common infaunal benthic foraminiferal taxa across the study interval. 1a-b: *Pleurostomella* sp. 1, sample U1508C, 22R (1, 109–110 cm); 2a-b: *Pleurostomella* sp. 2, sample U1508C, 22R (4, 58–59 cm); 3: polymorphinid, sample U1508C, 22R (1, 137–138 cm); 4: polymorphinid, sample U1508C, 22R (2, 119–120 cm); 5a-b: *Pullenia bulloides,* sample U1508C, 22R (1, 81–82 cm); 6a-b: *Pullenia quinqueloba,* sample U1508C, 22R (1, 15–16 cm)*;* 7: Uniserial agglutinated, sample U1508C, 22R (1, 15–16 cm); 8a-b: *Pyramidina* sp., sample U1508C, 22R (3, 5–6 cm); 9a-b: *Uvigerina peregrina*, sample U1508C, 22R (3, 120–121.5 cm); 10: agglutinated uniserial*,* sample U1508C, 22R (2, 119–120 cm)*;* 11 a-b: *Turrillina brevispira,* sample U1508C, 22R (2, 119–120 cm)*;* 12a-b: *Spiroplectammina spectabilis,* sample U1508C, 22R (2, 97–98 cm)*;* 13a-c*:* stilostomellid, sample U1508C, 22R (1, 15–16 cm)*;* 14a-b: biserial-triserial agglutinated, sample U1508C, 22R (5, 66–67 cm); 15a-b: *Karreriella bradyi,* sample U1508C, 22R (5, 66–67 cm). All scale bars = 100 μm.

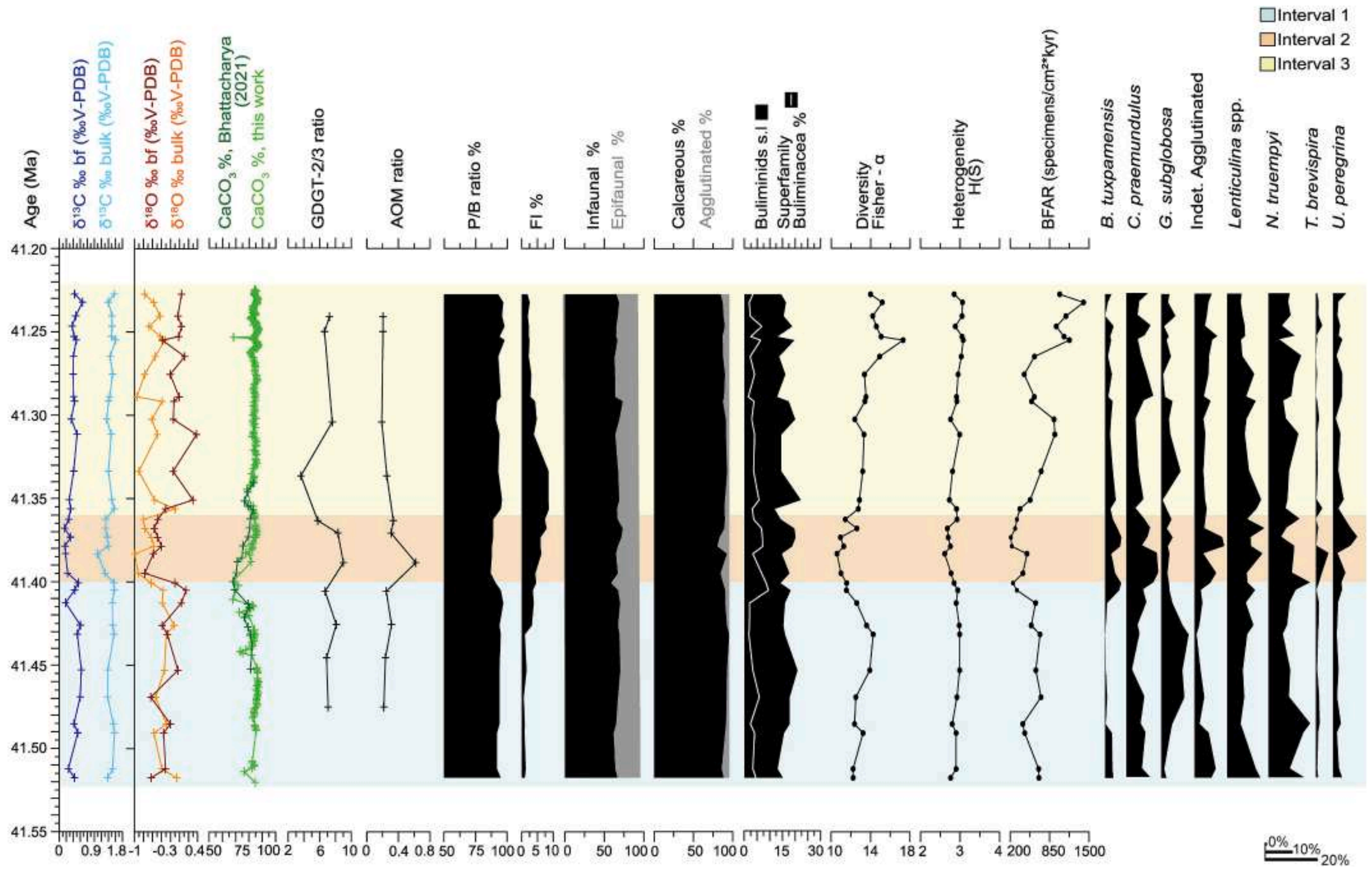

Fig. 10. Summary of the geochemical and faunal indices across the study interval at IODP Site U1508, plotted against age (Ma): carbon and oxygen stable isotopes, $CaCO_3$%, organic geochemistry (GDGT-2/3ratio (GDGT-2/GDGT-3), AOM ratio (GDGT-2/Cren)), planktonic/benthic foraminifera (P/B) ratio, fragmentation index (FI) of planktonic foraminifera, benthic foraminiferal groups and diversity indices, benthic foraminiferal accumulation rates (BFAR), and relative abundance of relevant benthic foraminiferal taxa.

1978; Jorissen et al., 2007; Stassen et al., 2012) (Figs. 5, 10). The assemblage includes common agglutinated biserial-triserial species, *Uvigerina peregrina*, *B. tuxpamensis* and other buliminids (in particular, *Turrillina brevispira*) (Figs. 6, 10), a group that tolerates reduced oxygen concentrations in the modern oceans (Sen Gupta and Machain-Castillo, 1993; Bernhard et al., 1997). Preservation of foraminiferal tests in Interval 2 is poor and may indicate slightly $CaCO_3$-corrosive bottom waters (but no dissolution), and oxygen deficiency. The abundance of *B. tuxpamensis* and *Cibicidoides* spp. during an early Eocene hyperthermal at Tasman Sea Site U1510 (Alegret et al., 2021b) supports their resilience to rapid warming events. Decreased oxygenation of bottom waters is also supported by the decrease in the relative abundance of the oxic indicator *Globocassidulina subglobosa* (Figs. 5, 10) (Bernhard, 1986; Corliss and Chen, 1988; Jorissen et al., 2007; Palmer et al., 2020). Oxygen deficiency and increased water stratification are supported by the high AOM ratio (GDGT2/Cren, a proxy for contribution by anaerobic methane-oxidiser) and increased GDGT2/3 values (Fig. 10).

Increased diversity and heterogeneity of the assemblages in the upper half of the LLTM (Interval 2) (Figs. 6, 10) indicate more favourable conditions in the deep-sea, likely related to improved oxygenation and a higher $CaCO_3$ saturation of bottom waters. FI values reach 8.64 % (Figs. 6, 10), and are significantly lower than the threshold value (15 %) that marks significant $CaCO_3$ dissolution (Kucera et al., 1997). Additionally, the slightly increased FI does not correlate with the increased $CaCO_3$% and with the dominance of calcareous taxa (Figs. 6, 10).

Decreased BFARs during the LLTM (Interval 2) point to lower export productivity and oligotrophic conditions at the seafloor. This interpretation is compatible with the increased stratification in the water column; alternatively, it might be related to a higher remineralization of the organic matter in the water column under warmer temperatures (Alegret et al., 2021b; Boscolo-Galazzo et al., 2021; John et al., 2013; Ma et al., 2014).

Interval 3 (564.51–560.96 m CSF-A) is characterised by the recovery of the P/B ratio to pre-event values, and the diversity and heterogeneity of benthic foraminiferal assemblages even reach higher values, indicating favourable conditions for the deep-sea benthos (Figs. 6, 10). The slight increase in the percentage of *G. subglobosa*, as compared to Interval 2, points to a higher oxygen content, and the higher percentage of stilostomellids suggests less stratified bottom waters and enhanced delivery of organic particles to these suspension feeders (Hottinger, 2000, 2006; Mancin et al., 2013; Alegret et al., 2021b). The FI values decrease, and together with the high $CaCO_3$ content, they indicate the return to a $CaCO_3$ saturation state similar to background values in Interval 1.

The increase in BFARs across Interval 3 indicates higher export productivity, and the return to meso-oligotrophic conditions. The epifaunal species *A. dissonata* has been reported to be a phytodetritus exploiting taxon (Van Morkhoven et al., 1986) associated with transient input of phytodetritus, but its low abundance at Site U1508 prevents us from further interpretations on this taxon.

5.3. The global signal of the LLTM

The identification of the LLTM at Site U1508 allows for comparison of its record in the Tasman Sea with the records available in the Atlantic Ocean, including the previously documented ODP Sites 702, 1260 and 1263 (Rivero-Cuesta et al., 2020; Westerhold et al., 2018) and the Cape Oyambre section (northern Spain; Intxauspe-Zubiaurre et al., 2018).

The LLTM was first described in the equatorial Atlantic Ocean, at

Ocean Drilling Program (ODP) Site 1260 (Demerara Rise; Edgar et al., 2007; Westerhold and Röhl, 2013), as a short-lived event marked by a decrease in $\delta^{13}C$ and $\delta^{18}O$ values and in (%) $CaCO_3$ content, and associated with $CaCO_3$ dissolution in the deep sea, as inferred from a distinct peak in XRF scanning Fe intensities and an increase in clay content. The event was also documented in the South Atlantic Ocean ODP Site 702 (Islas Orcadas Rise) and ODP Site 1263 (Walvis Ridge) (Westerhold et al., 2018). The three sites show the pronounced peak in Fe intensity accompanied by the negative CIE and OIE, and the decrease in $CaCO_3$%.

Studying the impact of the LLTM in the deep sea is essential for understanding how extreme warming by exceptionally strong insolation affects the climate system dynamics, but so far the response of benthic foraminifera has only been reported from two sites: the middle bathyal Cape Oyambre section (northeast Atlantic; Intxauspe-Zubiaurre et al., 2018), and the lower bathyal ODP Site 702 (South Atlantic; Rivero-Cuesta et al., 2020). In both studies, the event is marked by the negative CIE and OIE, as well as a decrease in carbonate content in deep-sea sediments. Intxauspe-Zubiaurre et al. (2018) documented the dominance of clay minerals and quartz grains across the LLTM, and sea-surface eutrophication triggered by enhanced continental nutrient discharge. These results agree with the study of Westerhold and Röhl (2013), which suggested an increased hydrological cycle as a consequence of exceptionally strong insolation at 41.5 Ma. Both studies of the benthic foraminiferal reponse to the LLTM reported a decrease in the diversity of the assemblages and temporary changes in the relative abundance of the species. Intxauspe-Zubiaurre et al. (2018) related the faunal turnover in the northeast Atlantic to increased organic matter export to the seafloor under oxic conditions (e.g. increased relative abundance of bi-triserial taxa or the species *Globocassidulina subglobosa*, and decreased relative abundance of *Nuttallides truempyi*), while Rivero-Cuesta et al. (2020) linked the changes in benthic foraminiferal assemblages (e.g. increased relative abundance of *Oridorsalis umbonatus* and decreased relative abundance of *Bulimina elongata*) to changes in the type of organic matter reaching the seafloor in the South Atlantic (Rivero-Cuesta et al., 2020).

At Site U1508 we estimated a duration of 30 kyr for the event, similar to the one reported in the Atlantic Ocean records (Westerhold et al., 2020). The apparent, minor discrepancies in the age of the LLTM (41.52 Ma in the Atlantic vs. 41.39 Ma in the southwest Pacific) are likely related to the different methods used to build the age models. The age model at Site U1508 is based on the assumption that linear sedimentation rates were constant between successive bio-magnetostratigraphic tie points, while the Atlantic studies are based on an astronomical tuned cyclostratigraphic age model. In addition, Site U1508 was rotary drilled, which causes sediment loss, and there are no cyclostratigraphy or astrochronology data. Although the lack of vertical gradient of oxygen isotopes suggests they have been overprinted by diagenesis, the negative shifts in $\delta^{18}O_{bulk}$ and $\delta^{18}O_{benthic}$ recorded at Site U1508 show values consistent with the excursions in the Atlantic Ocean, suggesting warmer surface and bottom waters during the LLTM in both ocean basins.

Changes in bottom water oxygenation or in the trophic conditions across the LLTM also differ among these studies. At Site U1508, benthic foraminifera and GDGTs suggest oxygen deficiency during the LLTM, and increased stratification of the water column. In contrast, no evidence for decreased oxygenation has been reported from the two Atlantic sites. In the continental marginal setting of Cape Oyambre, calcareous nannofossil assemblages indicate increased trophic conditions, and benthic foraminifera also point to a higher input of organic matter to the seafloor (Intxauspe-Zubiaurre et al., 2018), while benthic foraminiferal assemblages from open ocean settings indicate a decrease in the organic matter export to the seafloor (Site 1508) or changes in the type of organic matter delivered to the seafloor in a general oligo-mesotrophic environment (Site 702B, Rivero-Cuesta et al., 2020). The different response to the LLTM at the three sites could be related to their palaeoceanographic settings, with organic matter export to the seafloor at sites near continental margins (such as the middle bathyal Cape Oyambre section) being influenced by changes in runoff and terrestrial input, while open ocean settings such as the lower bathyal sites 702B and U1508 may have been more oligotrophic, due to increased remineralization of the organic matter through the water column under warmer temperatures, and possibly exacerbated by increased water stratification in the Tasman Sea. The three sites thus show different responses to the same forcing factor, the warming of the LLTM, and their palaeoceanographic setting may account for the observed divergence. Further in-depth studies of the biotic response to the LLTM at different latitudes, palaeodepths and ocean settings will contribute to identify the main drivers of the biotic and palaeoenvironmental consequences of very rapid warming events.

6. Conclusions

This study documents the deep-sea benthic foraminiferal turnover across the Late Lutetian Thermal Maximum (LLTM) for the first time in the Tasman Sea, southwestern Pacific Ocean. At IODP Site U1508, this middle Eocene hyperthermal event is marked by a sharp negative excursion of $\delta^{18}O$ and $\delta^{13}C$ measured in bulk sediment and benthic foraminifera.

Decreased diversity and heterogeneity of benthic foraminiferal assemblages indicate environmental stress at the seafloor during the LLTM, likely related to oxygen deficiency as suggested by the high relative abundance of dysoxic benthic foraminiferal taxa and supported by organic geochemistry analyses (the high AOM ratio, related to the contribution of anaerobic methane oxidizers, or the GDGT-2/3 ratio, associated to stratification of the water column). Low BFAR values indicate decreased export productivity in the Tasman Sea during the short-lived LLTM, likely due to increased organic matter remineralization in the water column, driven by warming-induced stratification. This phenomenon resulted in oligotrophic conditions in the deep-sea throughout the event. We also infer slightly $CaCO_3$-corrosive bottom waters during the LLTM but no carbonate dissolution, as assemblages are strongly dominated by calcareous taxa.

The deep-sea expression of the LLTM at IODP Site U1508 can only be compared with two other existing records, and we conclude that differences in the palaeoceanographic setting may account for the response of benthic foraminiferal assemblages. At middle bathyal sites near continental margins, organic matter export to the seafloor may have been influenced by changes in runoff and terrestrial input, while lower bathyal open ocean settings may have been more oligotrophic. We propose this spatial heterogeneity should be taken into account in the interpretation of palaeoceanographic models, as different settings may have critically affected the response of deep-sea biota to rapid warming events.

CRediT authorship contribution statement

Irene Peñalver-Clavel: Writing – review & editing, Writing – original draft, Investigation, Formal analysis, Data curation, Conceptualization. **Claudia Agnini:** Writing – review & editing, Formal analysis, Data curation. **Thomas Westerhold:** Writing – review & editing, Formal analysis, Data curation. **Marlow J. Cramwinckel:** Writing – review & editing, Formal analysis, Data curation. **Edoardo Dallanave:** Writing – review & editing, Formal analysis, Data curation. **Joyeeta Bhattacharya:** Writing – review & editing, Formal analysis, Data curation. **Rupert Sutherland:** Writing – review & editing, Formal analysis, Data curation. **Laia Alegret:** Writing – review & editing, Formal analysis, Data curation.

Declaration of competing interest

The authors declare that they have no known competing financial interests or personal relationships that could have appeared to influence the work reported in this paper.

Data availability

Data generated in this study are published in zenodo (https://doi.org/10.5281/zenodo.13170668)

Acknowledgments

Project PID2019-105537RB-I00, funded by MCIN/AEI/10.13039/501100011033 and by "ERDF A way of making Europe." IP was supported by the Spanish Ministry of Science and Innovation (MCIN) (FPI grant PRE2020-092638). Additional funding was provided by the Deutsche Forschungsgemeinschaft (DFG, German Research Foundation) under Germany's Excellence Strategy – EXC-2077–390741603 to TW, by DFG grants 408178503 and 465492305 to ED, and by PRIN20222 project cod. MUR 2022T4XEBP and RETURN Extended Partnership, financed by the National Recovery and Resilience Plan – NRRP, Mission 4, Component 2, Investment 1.3 – D.D. 1243 2/8/2022, PE0000005 to CA. We acknowledge the use of Servicio General de Apoyo a la Investigación-SAI, Universidad de Zaragoza. This research used samples and data provided by the International Ocean Discovery Program (IODP).

Appendix A. Supplementary data

Supplementary data to this article can be found online at https://doi.org/10.1016/j.marmicro.2024.102390.

References

Agnini, C., Fornaciari, E., Raffi, I., Catanzariti, R., Pälike, H., Backman, J., Rio, D., 2014. Biozonation and biochronology of Paleogene calcareous nannofossils from low and middle latitudes. Newsl. Stratigr. 47 (2), 131–181. https://doi.org/10.1127/0078-0421/2014/0042.

Alegret, L., Thomas, E., 2001. Upper cretaceous and lower Paleogene benthic foraminifera from northeastern Mexico. Micropaleontology 47, 269–316.

Alegret, L., Thomas, E., 2009. Food supply to the seafloor in the Pacific Ocean after the cretaceous/Paleogene boundary event. Mar. Micropaleontol. 73, 105–116. https://doi.org/10.1016/j.marmicro.2009.07.005.

Alegret, L., Reolid, M., Vega Pérez, M., 2018. Environmental instability during the latest Paleocene at Zumaia: the bellwether of the PETM. Palaeogeogr. Palaeoclimatol. Palaeoecol. 497, 186–200.

Alegret, L., Arreguín-Rodríguez, G.J., Trasviña-Moreno, C.A., Thomas, E., 2021a. Turnover and stability in the deep sea: benthic foraminifera as tracers of Paleogene global change. Glob. Planet. Chang. 196, 103372 https://doi.org/10.1016/j.gloplacha.2020.103372.

Alegret, L., Harper, D.T., Agnini, C., Newsham, C., Westerhold, T., Cramwinckel, M.J., Dallanave, E., Dickens, G.R., Sutherland, R., 2021b. Biotic response to early eocene warming events: integrated record from offshore Zealandia, North Tasman Sea. Paleoceanogr. Paleoclimatol. 36, e2020PA004179 https://doi.org/10.1029/2020PA004179.

Arreguín-Rodríguez, G.J., Alegret, L., 2016. Deep-sea benthic foraminiferal turnover across early eocene hyperthermal events at Northeast Atlantic DSDP site 550. Palaeogeogr. Palaeoclimatol. Palaeoecol. 451, 62–72.

Arreguín-Rodríguez, G.J., Thomas, E., D'haenens, S., Speijer, R.P., Alegret, L., 2018. Early eocene deep-sea benthic foraminiferal faunas: recovery from the paleocene eocene thermal maximum extinction in a greenhouse world. PLoS ONE 13, e0193167.

Arreguín-Rodríguez, G.J., Thomas, E., Alegret, L., 2022. Some like it cool: benthic foraminiferal response to paleogene warming events. Palaeogeogr. Palaeoclimatol. Palaeoecol. 593, 110925 https://doi.org/10.1016/j.palaeo.2022.110925.

Baatsen, M., von der Heydt, A.S., Huber, M., Kliphuis, M.A., Bijl, P.K., Sluijs, A., Dijkstra, H.A., 2020. The Middle-to-Late Eocene Greenhouse Climate, Modelled Using the CESM 1.0.5, Climate of the Past Discussions. https://doi.org/10.5194/cp-2020-29.

Berger, W.H., Diester-Haass, L., 1988. Paleoproductivity: the benthic/planktonic ratio in foraminifera as a productivity index. Mar. Geol. 81, 15–25.

Berger, W.H., Bonneau, M.C., Parker, F.L., 1982. Foraminifera on the deep-sea floor: lysocline and dissolution rate. Oceanol. Acta 5, 249–258.

Bernhard, J.M., 1986. Characteristic assemblages and morphologies of benthic foraminifera from anoxic, organic-rich deposits: jurassic through holocene. J. Foraminifer. Res. 16 (3), 207–215.

Bernhard, J.M., Sen Gupta, B.K., Borne, P.F., 1997. Benthic foraminiferal proxy to estimate dysoxic bottom water oxygen concentrations, Santa Barbara Basin. US Pacific continental margin. J. Foraminifer. Res. 27, 301–310.

Bhattacharya, J., 2021. Marine Carbonate Accumulation during the Greenhouse Climate of the Eocene. Diss. Rice University.

Bhattacharya, J., Dickens, G.R., 2020. Eocene carbonate accumulation in the north-Central Pacific Ocean: new insights from Ocean Drilling Program Site 1209, Shatsky rise. Sediment. Geol. 405, 105705. ISSN 0037–0738. https://doi.org/10.1016/j.sedgeo.2020.105705.

Bignot, G., 1998. Middle Eocene benthic foraminifers from holes 960A and 960C, Central Atlantic Ocean. In: Mascle, J., Lohmann, G.P., Moullade, M. (Eds.), Proceedings of the Ocean Drilling Program. Texas A&M University, Scientific Results, pp. 433–444.

Bijl, P.K., Houben, A.J.P., Schouten, S., Bohaty, S.M., Sluijs, A., Reichart, G.-J., Damste, J.S.S., Brinkhuis, H., 2010. Transient middle eocene atmospheric CO2 and temperature variations. Science 330, 819–821.

Bijl, P.K., Pross, J., Warnaar, J., Stickley, C.E., Huber, M., Guerstein, R., Houben, A.J.P., Sluijs, A., Visscher, H., Brinkhuis, H., 2011. Environmental Forcings of Paleogene Southern Ocean Dinoflagellate Biogeography Department of Earth, Atmospheric, and Planetary Sciences Faculty Publications, Paper 174. docs.lib.purdue.edu/easpubs/174.

Bijl, P.K., Frieling, J., Cramwinckel, M.J., Boschman, C., Sluijs, A., Peterse, F., 2021. Maastrichtian–Rupelian paleoclimates in the southwest Pacific – a critical re-evaluation of biomarker paleothermometry and dinoflagellate cyst paleoecology at Ocean Drilling Program Site 1172. Clim. Past 17, 2393–2425. https://doi.org/10.5194/cp-17-2393-2021.

Bohaty, S.M., Zachos, J.C., 2003. Significant Southern Ocean warming event in the late middle Eocene. Geology 31, 1017–1020.

Boscolo-Galazzo, F., Crichton, K.A., Ridgwell, A., Mawbey, E.M., Wade, B.S., Pearson, P.N., 2021. Temperature controls carbon cycling and biological evolution in the ocean twilight zone. Science 371, 1148–1152. https://doi.org/10.1126/science.abb6643.

Buzas, M.A., Culver, S.J., Jorissen, F.J., 1993. A statistical evaluation of the microhabitats of living (stained) infaunal benthic foraminifera. Mar. Micropaleontol. 20, 311–320. https://doi.org/10.1016/0377-8398(93)90040-5.

Cao, W., Zahirovic, S., Flament, N., Williams, S., Golonka, J., Dietmar Müller, R., 2017. Improving global paleogeography since the late paleozoic using paleobiology. Biogeosciences 14 (23), 5425–5439. https://doi.org/10.5194/bg-14-5425-2017.

Corliss, B.H., 1991. Morphology and microhabitat preferences of benthic foraminifera from the Northwest Atlantic Ocean. Mar. Micropaleontol. 17, 195–236.

Corliss, B.H., Chen, C., 1988. Morphotype patterns of Norwegian Sea deep-sea benthic foraminifera and ecological implications. Geology 16, 716–719.

Cramwinckel, M.J., Woelders, L., Huurdeman, E.P., Peterse, F., Gallagher, S.J., Pross, J., Burgess, C.E., Reichart, G.-J., Sluijs, A., Bijl, P.K., 2020. Surface-circulation change in the Southwest Pacific Ocean across the middle eocene climatic optimum: inferences from dinoflagellate cysts and biomarker paleothermometry. Clim. Past 16, 1667–1689. https://doi.org/10.5194/cp-16-1667-2020.

Dallanave, E., Chang, L., 2020. Early eocene to early miocene magnetostratigraphic framework for IODP expedition 371 (tasman frontier subduction initiation and paleogene climate). Newsl. Stratigr. 53, 365–387. https://doi.org/10.1127/nos/2019/0556.

Dallanave, E., Sutherland, R., Dickens, G.R., Chang, L., Tema, E., Alegret, L., Agnini, C., Westerhold, T., Newsam, C., Lam, A.R., Stratford, W.R., Collot, J., Etienne, S.J.G., Von Dobeneck, T., 2022. Absolute paleolatitude of Northern Zealandia from the middle eocene to the early miocene. J. Geophys. Res. Solid Earth 127, 1–19. https://doi.org/10.1029/2022JB024736.

D'haenens, S., Bornemann, A., Stassen, P., Speijer, R.P., 2012. Multiple early eocene benthic foraminiferal assemblage and δ13C fluctuations at DSDP Site 401 (Bay of Biscay—NE Atlantic). Mar. Micropaleontol. 88–89, 15–35. https://doi.org/10.1016/j.marmicro.2012.02.006.

Dupont-Nivet, G., Van Hinsbergen, D.J.J., Torsvik, T.H., 2010. Persistently low Asian paleolatitudes: implications for the India-Asia collision history. Tectonics 29 (5), TC5016. https://doi.org/10.1029/2008TC002437.

Edgar, K.M., Wilson, P.A., Sexton, P.F., Suganuma, Y., 2007. No extreme bipolar glaciation during the main Eocene calcite compensationshift. Nature 448 (7156), 908–911. https://doi.org/10.1038/nature06053.

Fisher, R., 1953. Dispersion on a sphere. Proc. R. Soc. Lond. A217, 295–305.

Fontanier, C., Jorissen, F.J., Licari, L., Alexandre, A., Anschutz, P., Carbonel, P., 2002. Live benthic foraminiferal faunas from the Bay of Biscay: faunal density, composition and microhabitats. Deep-Sea Res. I 49, 751–785. https://doi.org/10.1016/s0967-0637(01)00078-4.

Foster, G.L., Hull, P., Lunt, D.J., Zachos, J.C., 2018. Placing our current 'hyperthermal' in the context of rapid climate change in our geological past. Phil. Trans. R. Soc. A 376, 20170086. https://doi.org/10.1098/rsta.2017.0086.

Gastaldello, M.E., Agnini, C., Alegret, L., 2024. Late miocene to early pliocene benthic foraminifera from the Tasman Sea (Integrated Ocean Drilling Program Site U1506). J. Micropalaeontol. 43, 1–35. https://doi.org/10.5194/jm-43-1-2024.

Gilabert, V., Arz, J.A., Arenillas, I., Robinson, S.A., 2021. Influence of the latest Maastrichtian warming event on planktonic foraminiferal assemblages and ocean carbonate saturation at Caravaca, Spain. Cretac. Res. 125, 104844 https://doi.org/10.1016/j.cretres.2021.104844.

Gooday, A.J., 2003. Benthic foraminifera (protista) as tools in deep-water palaeoceanography: environmental influences on faunal characteristics. Adv. Mar. Biol. 46, 1–90.

Gruber, N., 2011. Warming up, turning sour, losing breath: ocean biogeochemistry under global change. Philos. Trans. R. Soc. A Math. Phys. Eng. Sci. 369 (1943), 1980–1996. https://doi.org/10.1098/rsta.2011.0003.

Hankard, F., Cogné, J.P., Kravchinsky, V.A., Carporzen, L., Bayasgalan, A., Lkhagvadorj, P., 2007. New tertiary paleomagnetic poles from Mongolia and Siberia at 40, 30, 20, and 13 Ma: clues on the inclination shallowing problem in Central Asia. J. Geophys. Res. Solid Earth 112 (2). https://doi.org/10.1029/2006JB004488.

Harlan, S.S., Geissman, J.W., Henry, C.D., Onstott, T.C., 1995. Paleomagnetism and 40Ar/39Ar geochronology of gabbro sills at Mariscal Mountain anticline, southern big Bend National Park, Texas: implications for the timing of Laramide tectonism and vertical axis rotations in the southern Cordilleran orogenic belt. Tectonics 14 (2), 307–321. https://doi.org/10.1029/94TC03089.

Hayward, B.W., Carter, R., Grenfell, H.R., Hayward, J.J., 2001. Depth distribution of recent deep-sea benthic foraminifera east of New Zealand, and their potential for improving paleobathymetric assessments of Neogene microfaunas. N. Z. J. Geol. Geophys. 44, 555–587.

Hayward, B.W., Grenfell, H.R., Carter, R., Hayward, J.J., 2004. Benthic foraminiferal proxy evidence for the Neogene palaeoceanographic history of the Southwest Pacific, east of New Zealand. Mar. Geol. 205, 147–184.

Hayward, B.W., Grenfell, H.R., Sabaa, A.T., Neil, H., Buzas, M.A., 2010. Recent New Zealand deepwater benthic foraminifera: taxonomy, ecologic distribution, biogeography, and use in paleoenvironmental assessment. GNS Sci. Monogr. 26, 363 (Lower Hutt, New Zealand).

Hayward, B.W., Kawagata, S., Sabaa, A.T., Grenfell, H.R., van Kerckhoven, L., Johnson, K., Thomas, E., 2012. The Last Global Extinction (Mid-Pleistocene) of Deep-Sea Benthic Foraminifera (Chrysalogoniidae, Ellipsoidinidae, Glandulonodosariidae, Plectofrondiculariidae, Pleurostomellidae, Stilostomellidae), Their Late Cretaceous-Cenozoic History and Taxonomy, Vol. 43. Cushman Foundation for Foraminiferal Research Special Publication, p. 408.

Herguera, J.C., 2000. Last glacial paleoproductivity patterns in the eastern equatorial Pacific: benthic foraminifera records. Mar. Micropaleontol. 40, 259–274.

Herguera, J.C., Berger, W.H., 1991. Paleoproductivity from benthic foraminifera abundance: glacial to postglacial change in the West-Equatorial Pacific. Geology 19, 1173–1176.

Holbourn, A., Henderson, A.S., MacLeod, N., 2013. Atlas of Benthic Foraminifera, Natural History Museum, London. Wiley-Blackwell.

Hopmans, E.C., Weijers, J.W.H., Schefuß, E., Herfort, L., Sinninghe Damsté, J.S., Schouten, S., 2004. A novel proxy for terrestrial organic matter in sediments based on branched and isoprenoid tetraether lipids. Earth Planet. Sci. Lett. 224, 107–116.

Hottinger, L.C., 2000. Functional morphology of benthic foraminiferal shells, envelopes of cells beyond measure. Micropaleontology 46 (1), 57–86.

Hottinger, L.C., 2006. The “face” of benthic foraminifera. Boll. Soc. Paleontol. Ital. 45, 75–89.

Huber, M., Brinkhuis, H., Stickley, C.E., Döös, K., Sluijs, A., Warnaar, J., Schellenberg, S. A., Williams, G.L., 2004. Eocene circulation of the Southern Ocean: was Antarctica kept warm by subtropical waters? Paleoceanography 19 (4). https://doi.org/10.1029/2004pa001014.

Intxauspe-Zubiaurre, B., Martinez-Braceras, N., Payros, A., Ortiz, S., Dinares-Turell, J., Flores, J.A., 2018. The last Eocene hyperthermal (Chron C19r event, ~41.5 Ma): chronological and paleoenvironmental insights from a continental margin (Cape Oyambre, N Spain). Palaeogeogr. Palaeoclimatol. Palaeoecol. 505, 198–216.

Irving, E., Baker, J., Wynne, P.J., Hamilton, T.S., Wingate, M.T.D., 2000. Evolution of the Queen Charlotte Basin: further paleomagnetic evidence of Tertiary extension and tilting. Tectonophysics 326 (1–2), 1–22. https://doi.org/10.1016/S0040-1951(00)00143-8.

John, E.H., Pearson, P.N., Coxall, H.K., Birch, H., Wade, B.S., Foster, G.L., 2013. Warm ocean processes and carbon cycling in the Eocene. Philos. Trans. R. Soc. A Math. Phys. Eng. Sci. 371, 20130099 https://doi.org/10.1098/rsta.2013.0099.

Jones, R.W., Charnock, M.A., 1985. “Morphogroups” of agglutinated foraminifera. Their life positions and feeding habits and potential applicability in (paleo)ecological studies. Rev. Paléobiol. 4 (2), 311–320.

Jorissen, F.J., Stigter, H.C., Widmark, J.G.V., 1995. A conceptual model explaining benthic foraminiferal microhabitats. Mar.Micropaleontol. 26, 3–15.

Jorissen, F.J., Fontanier, C., Thomas, E., 2007. Chapter seven Paleoceanographical proxies based on deep-sea benthic foraminiferal assemblage characteristics. Dev. Mar. Geol. 1 (07), 263–325. https://doi.org/10.1016/S1572-5480(07)01012-3.

Kaminski, M.A., Gradstein, F.M., 2005. Cenozoic cosmopolitan deep-water agglutinated foraminifera. Grzybowski Foun. Spec. Publ. 10, 547.

Katz, M.E., Tjalsma, R.C., Miller, K.G., 2003. Oligocene bathyal to abyssal benthic foraminifera of the Atlantic Ocean. Micropaleontology 49, 1–45.

Kawahata, H., Nomura, R., Matsumoto, K., Nishi, H., 2015. Linkage of deep sea rapid acidification process and extinction of benthic foraminifera in the deep sea at the paleocene/eocene transition. Island Arc 24, 301–316. https://doi.org/10.1111/iar.12106.

Kennett, J.P., 1977. Cenozoic evolution of Antarctic glaciation, circum-Antarctic Ocean, and their impact on global paleoceanography. J. Geophys. Res. Oceans Atmos. 82 (27), 3843–3860. https://doi.org/10.1029/JC082i027p03843.

Kirschvink, J.L., 1980. The least-squares line and plane and the analysis of palaeomagnetic data. Geophys. J. R. Astron. Soc. 62 (3), 699–718. https://doi.org/10.1111/j.1365-246X.1980.tb02601.x.

Kucera, M., Malmgren, B.A., Sturesson, U., 1997. Foraminiferal dissolution at shallow depths of the Walvis Ridge and Rio Grande rise during the latest cretaceous: inferences for deep-water circulation in the South Atlantic. Palaeogeogr. Palaeoclimatol. Palaeoecol. 129 (3–4), 195–212. https://doi.org/10.1016/S0031-0182(96)00133-2.

Leon-Rodriguez, L., Dickens, G.R., 2010. Constraints on ocean acidification associated with rapid and massive carbon injections: the early Paleogene record at ocean drilling program site 1215, equatorial Pacific Ocean. Palaeogeogr. Palaeoclimatol. Palaeoecol. 298, 409–420.

Loeblich Jr., A.R., Tappan, H., 1987. Foraminiferal Genera and their Classification. Van Nostrand Reinhold Company, pp. 1–2.

Lohmann, G.P., 1978. Abyssal benthonic foraminifera as hydrographic indicators in the western South Atlantic Ocean. J. Foraminifer. Res. 8, 6–34.

Lyle, M., Lyle, A.O., Backman, J., Tripati, A.K., 2005. Biogenic sedimentation in the eocene equatorial pacific - the stuttering greenhouse and eocene carbonate compensation depth. Proc. Ocean Drilling Prog. Sci. Results 199, 1–35.

Ma, Z., Gray, E., Thomas, E., Murphy, B., Zachos, J.C., Paytan, A., 2014. Carbon sequestration during the paleocene-eocene termal maximum by an efficient biological pump. Nat. Geosci. 7, 382–388. https://doi.org/10.1038/NGEO2139.

Mancin, N., Hayward, B.W., Trattenero, I., Cobianchi, M., Lupi, C., 2013. Can the morphology of deep-sea benthic foraminifera reveal what caused their extinction during the mid-pleistocene climate transition? Mar. Micropaleontol. 104, 53–70. https://doi.org/10.1016/j.marmicro.2013.09.004.

Mead, G.A., 1985. Recent benthic foraminifera in the polar front region of the Southwest Atlantic. Micropaleontology 31, 221–248.

Mortimer, N., Campbell, H.J., Tulloch, A.J., King, P.R., Stagpoole, V.M., Wood, R.A., Rattenbury, M.S., Sutherland, R., Adams, C.J., Collot, J., 2017. Zealandia: earth’s hidden continent. GSA Today 27 (3). https://doi.org/10.1130/GSATG321A.1.

Mullender, T.A.T., Frederichs, T., Hilgenfeldt, C., de Groot, L.V., Fabian, K., Dekkers, M. J., 2016. Automated pa-leomagnetic and rock magnetic data acquisition with anin-line horizontal “2G” system. Geochem. Geophys. Geosyst. 17, 1–14. https://doi.org/10.1002/2016GC006436.

Müller, R.D., Seton, M., Zahirovic, S., Williams, S.E., Matthews, K.J., Wright, N.M., Shephard, G.E., Maloney, K.T., Barnett-moore, N., Hosseinpour, M., Bower, D.J., Cannon, J., 2016. Ocean Basin evolution and global-scale plate reorganization events since pangea breakup. Annu. Rev. Earth Planet. Sci. 44, 107–138.

Müller, R.D., Cannon, J., Qin, X., Watson, R.J., Gurnis, M., Williams, S., Pfaffelmoser, T., Seton, M., Russell, S.H.J., Zahirovic, S., 2018a. GPlates: building a virtual earth through deep time. Geochem. Geophys. Geosyst. 19, 2243–2261.

Murray, J.W., 1991. Ecology and Paleoecology of Benthic Foraminifera. Longman, Harlow, pp. 1–397.

Ortiz, S., Thomas, E., 2015. Deep-sea benthic foraminiferal turnover during the early–middle eocene transition at Walvis Ridge (SE Atlantic). Palaeogeogr. Palaeoclimatol. Palaeoecol. 417, 126–136.

Palmer, H.M., Hill, T.M., Roopnarine, P.D., Myhre, S.E., Reyes, K.R., Donnenfield, J.T., 2020. Southern California margin benthic foraminiferal assemblages record recent centennial-scale changes in oxygen minimum zone. Biogeosciences 17 (11), 2923–2937. https://doi.org/10.5194/bg-17-2923-2020.

Pearson, P.N., 2010. Increased atmospheric CO2 during the middle eocene. Science 330, 763–764.

Pflum, C.E., Frerichs, W.E., 1976. Gulf of Mexico Deepwater Foraminifers: Cushman Foundation for Foraminiferal Research Special Publication, 14, pp. 7–125.

Ressetar, R., Martin, D.L., 1980. Paleomagnetism of eocene igneous intrusions in the valley and Ridge Province, Virginia and West Virginia. Can. J. Earth Sci. 17 (11), 1583–1588. https://doi.org/10.1139/e80-165.

Rivero-Cuesta, L., Westerhold, T., Alegret, L., 2020. The late Lutetian thermal Maximum (middle Eocene): first record of deep-sea benthic foraminifera response. Palaeogeogr. Palaeoclimatol. Palaeoecol. 545, 109637.

Schmidt, A.G., Riisager, P., Abrahamsen, N., Riisager, J., Pedersend, A.K., Van der Voo, R., 2005. Palaeomagnetism of eocene talerua member lavas on hareøen, West Greenland. Bull. Geol. Soc. Den. 52, 27–38.

Schouten, S., Hopmans, E.C., Sinninghe Damste, J.S., 2013. The organic geochemistry of glycerol dialkyl glycerol tetraether lipids: a review. Org. Geochem. 54, 19–61.

Sen Gupta, B.K., 1999. Introduction to modern foraminifera. In: Sen Gupta, B.K. (Ed.), Systematics of Modern Foraminifera. Kluwer Academic Publishers, pp. 7–36. https://doi.org/10.1007/0-306-48104-9_2.

Sen Gupta, B.K., Machain-Castillo, M.L., 1993. Benthic foraminifera in oxygen-poor habitats. Mar. Micropaleontol. 20, 183–201.

Sexton, P.F., Norris, R.D., Wilson, P.A., Pälike, H., Westerhold, T., Röhl, U., Bolton, C.T., Gibbs, S., 2011. Eocene global warming events driven by ventilation of oceanic dissolved organic carbon. Nature 471, 349–352.

Sheriff, S.D., Shive, P.N., 1980. Paleomagnetism of the Leucite Hills volcanic field, southwestern Wyoming. Geophys. Res. Lett. 7 (12), 1025–1028. https://doi.org/10.1029/GL007i012p01025.

Sijp, W.P., von der Heydt, A.S., Dijkstra, H.A., Flögel, S., Douglas, P.M.J., Bijl, P.K., 2014. The role of ocean gateways on cooling climate on long time scales. Glob. Planet. Chang. 119, 1–22. https://doi.org/10.1016/j.gloplacha.2014.04.004.

Stassen, P., Steurbaut, E., Morsi, A.M., Schulte, P., Speijer, R., 2012. Biotic impact of eocene thermal maximum 2 in a shelf 720 setting (Dababiya, Egypt). Austr. J. Earth Sci. 105 (1), 154–160.

Sutherland, R., Dickens, G.R., Blum, P., Agnini, C., Alegret, L., Asatryan, G., et al., 2019. Expedition 371 methods. Proc. Int. Ocean Discov. Prog. 371, 1–65. https://doi.org/10.14379/iodp.proc.371.2019.

Sutherland, R., Dickens, G.R., Blum, P., Agnini, C., Alegret, L., Asatryan, G., Bhattacharya, J., Bordenave, A., Chang, L., Collot, J., Cramwinckel, M.J., Dallanave, E., Drake, M.K., Etienne, S.J.G., Giorgioni, M., Gurnis, M., Harper, D.T., Huang, H.-H.M., Keller, A.L., Zhou, X., 2020. Continental-scale geographic change across Zealandia during paleogene subduction initiation. Geology 48 (5), 419–424. https://doi.org/10.1130/G47008.1.

Symons, D.T.A., Erdmer, P., McCausland, P.J.A., 2003. A new cratonic north American paleomagnetic pole from the Yukon shows post-Eocene mobility of the Canadian Cordilleran terranes. Can. J. Earth Sci. 40, 1321–1334.

Takeda, K., Kaiho, K., 2007. Faunal turnovers in Central Pacific benthic foraminifera during the paleocene-eocene thermal maximum. Palaeogeogr. Palaeoclimatol. Palaeoecol. 251, 175–197. https://doi.org/10.1016/j.palaeo.2007.02.026.

Taylor, K.W.R., Huber, M., Hollis, C.J., Hernandez Sanchez, M.T., Pancost, R.D., 2013. Re-evaluating modern and palaeogene GDGT distributions: implications for SST reconstructions. Glob. Planet. Chang. 108, 158–174. https://doi.org/10.1016/j.gloplacha.2013.06.011.

Thomas, E., 1990. Late cretaceous – early eocene mass extinctions in the deep sea. Geol. Soc. Am. Spec. Pap. 247, 481–495.

Thomas, E., 1992. Middle eocene-late oligocene bathyal benthic foraminifera (Weddell Sea): faunal changes and implications for ocean circulation. In: Prothero, D.R., Berggren, W.A. (Eds.), Eocene-Oligocene Climatic and Biotic Evolution. Princeton University Press, pp. 245–271.

Thomas, E., Zachos, J.C., Bralower, T.J., 2000. Deep-Sea Environments on a Warm Earth: Latest Paleocene-Early Eocene. In: Huber, B.T., Macleod, K.G., Wing, S.L. (Eds.), Warm Climates in Earth History. Cambridge University Press, pp. 132–160.

Tjalsma, R.C., Lohmann, G.P., 1983. Paleocene-eocene bathyal and abyssal benthic foraminifera from the Atlantic Ocean. 4. Micropaleontology special. Publication 1–89.

Vaes, B., van Hinsbergen, D.J.J., van de Lagemaat, S.H.A., van der Wiel, E., Lom, N., Advokaat, E., et al., 2023. A global apparent polar wander path for the last 320 Ma calculated from site-level paleomagnetic data. Earth Sci. Rev. 245 (104547), 1–35. https://doi.org/10.1016/j.earscirev.2023.104547.

van der Weijst, C.M.H., Winkelhorst, J., de Nooijer, W., von der Heydt, A., Reichart, G.-J., Sangiorgi, F., Sluijs, A., 2022. Pliocene evolution of the tropical Atlantic thermocline depth. Clim. Past 18, 961–973. https://doi.org/10.5194/cp-18-961-2022.

Van der Zwaan, G.J., Jorissen, F.J., y De Stigter, H. C., 1990. The depth dependency of planktonic/benthic foraminiferal ratios; constraints and applications. Mar. Geol. 95, 1–16.

Van Morkhoven, F.P.C.M., Berggren, W.A., Edwards, A.S., 1986. Cenozoic cosmopolitan deep-water benthic foraminifera: Pau, France. Bull. Centre Recher. Explor. Prod. -Aquit. 11, 421.

Wade, B.S., Kroon, D., 2002. Middle Eocene regional climate instability: evidence from the western North Atlantic. Geology 30, 1011–1014.

Weijers, J.W.H., Lim, K.L.H., Aquilina, A., Damsté, J.S.S., Pancost, R.D., 2011. Biogeochemical controls on glyceroldialkyl glycerol tetraether lipid distributions in sediments characterized by diffusive methane flux. Geochem. Geophys. Geosyst. 12, GC003724 https://doi.org/10.1029/2011GC003724.

Westerhold, T., Röhl, U., 2013. Orbital pacing of Eocene climate during the Middle eocene climate optimum and the chron C19r event: missing link found in the tropical western Atlantic: orbital pacing of eocene climate. Geochem. Geophys. Geosyst. 14, 4811–4825.

Westerhold, T., Röhl, U., Donner, B., Frederichs, T., Kordesch, W.E.C., Bohaty, S.M., Zeebe, R.E., 2018. Late lutetian thermal maximum-crossing a thermal threshold in earth's climate system? Geochem. Geophys. Geosyst. 19, 73–82. https://doi.org/10.1002/2017GC007240.

Westerhold, T., Marwan, N., Drury, A.J., Liebrand, D., Agnini, C., Anagnostou, E., Barnet, J.S.K., Bohaty, S.M., De Vleeschouwer, D., Florindo, F., Frederichs, T., Hodell, D.A., Holbourn, A.E., Kroon, D., Lauretano, V., Littler, K., Lourens, L.J., Lyle, M., Pälike, H., Röhl, U., Tian, J., Wilkens, R.H., Wilson, P.A., Zachos, J.C., 2020. An astronomically dated record of earth's climate and its predictability over the last 66 million years. Science 369 (6509), 1383–1387. https://doi.org/10.1126/science.aba6853.

Zhang, Y.G., Zhang, C.L., Liu, X.-L., Li, L., Hinrichs, K.U., Noakes, J.E., 2011. Methane index: a tetraether archaeal lipidbiomarker indicator for detecting the instabilityofmarine gas hydrates. Earth Planet. Sci. Lett. 307, 525–534. https://doi.org/10.1016/j.epsl.2011.05.031.

Zijderveld, J.D.A., 1967. A.C. Demagnetization of rocks: analysis of results. In: Collinson, D.W., Creer, K.M., Runcorn, S.K. (Eds.), Methods in Paleomagnetism. Elsevier, New York, pp. 254–286.